Key Points:
- The 2017 Sarpol-e-Zahab earthquake ruptured a nearly NS trending fault, with most of moment release well beneath the sedimentary cover
- Large postseismic deformation 1 year after the earthquake is well explained by afterslip both updip and downdip of the coseismic rupture
- Postseismic deformation data indicate distinct frictional properties updip and downdip of the coseismic rupture

Supporting Information:
- Supporting Information S1

Correspondence to:
K. Wang,
kjellywang@gmail.com

Probing Fault Frictional Properties During Afterslip Updip and Downdip of the 2017 *Mw* 7.3 Sarpol-e Zahab Earthquake With Space Geodesy

Kang Wang[1] and Roland Bürgmann[1]

[1]Department of Earth and Planetary Sciences, University of California, Berkeley, CA, USA

Abstract We use interferometric synthetic aperture radar (InSAR) data collected by the Sentinel-1 mission to study the coseismic and postseismic deformation due to the 2017 *Mw* 7.3 Sarpol-e Zahab earthquake that occurred near the Iran-Iraq border in Northwest Zagros. We find that most of the coseismic moment release is between 15- and 21-km depths, well beneath the boundary between the sedimentary cover and underlying basement. Data from four satellite tracks reveal robust postseismic deformation during ~12 months after the mainshock (from November 2017 to December 2018). Kinematic inversions show that the observed postseismic InSAR line-of-sight (LOS) displacements are well explained by oblique (thrust + dextral) afterslip both updip and downdip of the coseismic peak slip area. The dip angle of the shallow afterslip fault plane is found to be significantly smaller than that of the coseismic rupture, corresponding to a shallowly dipping detachment located near the base of the sediments or within the basement, depending on the thickness of the sedimentary cover, which is not well constrained over the epicentral area. Aftershocks during the same time period exhibit a similar temporal evolution as the InSAR time series, with most of aftershocks being located within and around the area of maximum surface deformation. The postseismic deformation data are consistent with stress-driven afterslip models, assuming that the afterslip evolution is governed by rate-strengthening friction. The inferred frictional properties updip and downdip of the coseismic rupture are significantly different, which likely reflect differences in fault zone material at different depths along the Zagros.

1. Introduction

With a total length of more than 1,000 km, the Zagros Mountains in southwestern Iran are one of the major seismically active orogens in the world. The active deformation is a consequence of the ongoing continental collision between the Arabian and Eurasian plates, which initiated 10–35 Ma ago (e.g., Hessami et al., 2001; McQuarrie et al., 2003; Pirouz et al., 2017). The current plate convergence rate is ~20–30 mm/year, of which approximately one third is accommodated by a series of folds and thrusts within the mountain range, with the remainder being mainly accommodated by the Alborz, Greater Caucasus, and Kopet Dag mountain ranges to the north (Masson et al., 2005; Vernant et al., 2004) and subduction of the South Caspian Basin further to the north (Hollingsworth et al., 2008). Shallow folding and thrusting in the Zagros involve an 8- to 14-km-thick sedimentary cover that spans the entire Phanerozoic, overlying crystalline basement hosting seismically active thrust faults (e.g., Berberian., 1995). A weak detachment horizon may lie at the base of the sedimentary sequence, possibly rooted in thick evaporite deposits that outcrop in diapirs in the SE Zagros (Jahani et al., 2007; McQuarrie, 2004). Based on distinct characteristics of topography, geomorphology, stratigraphy, and seismicity, the Zagros range can be divided into two zones: the ~200-km-wide High Zagros to the northeast that averages 1.5–2 km in elevation and the Simply Folded Belt (SFB) that lies along the frontal part of the mountain range. The SFB is further subdivided along strike into the mountainous Lurestan and Fars arcs and the low-lying Kirkuk and Dezful embayments. Despite the relatively rapid shortening across the Zagros, there is no evidence of historical surface-rupturing earthquakes in the SFB. The largest instrumentally recorded earthquakes along the Zagros were the 1972 Ghir and the 1977 Khurgu earthquakes in the Fars arc in southeastern Zagros, both of which were estimated to be approximately *Mw* 6.7 (Nissen et al., 2011).

On 12 November 2017 at 18:18 UTC (local time 19:18), a *Mw* 7.3 earthquake struck the northwestern portion of the SFB in the Lurestan arc, causing a total of more than 600 fatalities in Iran and Iraq. The epicenter of
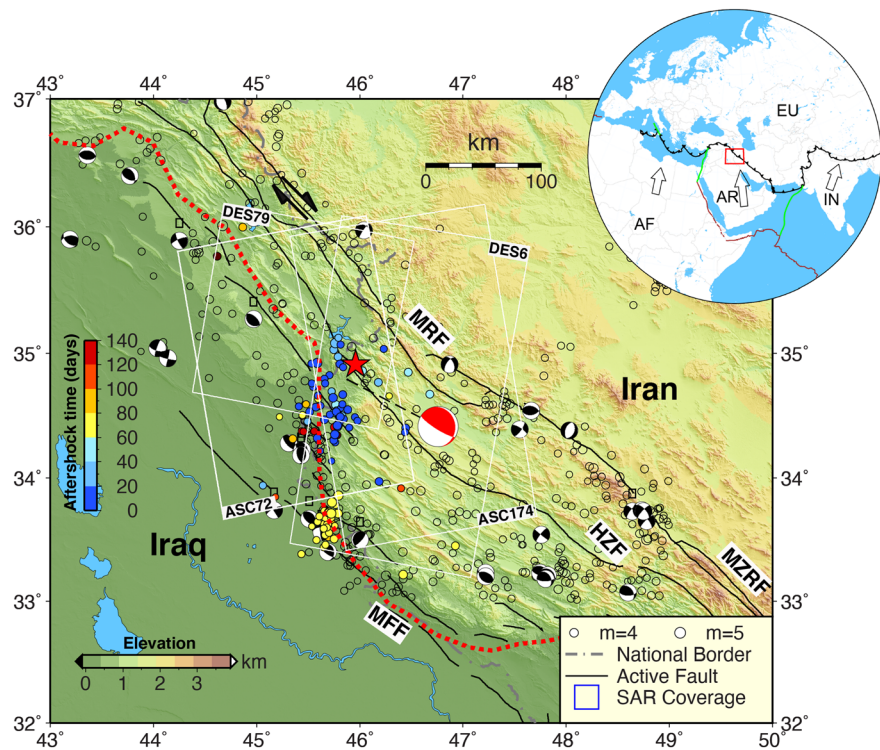
Figure 1. Tectonic setting of the 2017 *Mw* 7.3 Sarpol-e Zahab earthquake. Black line represents the active blind faults in this area inferred from structural and stratigraphic relations. Red star indicates the epicenter of the mainshock. Black beach balls represent the locations and focal mechanisms of M ≥ 4.5 earthquakes, from 1976–2017 (https://www. globalcmt.org). Inset shows the tectonic setting of the study area. Solid circles represent the *M* > 4 aftershocks catalogued by U.S. Geological Survey (USGS) during ~5 months after the mainshock, colored by the time since the mainshock. White boxes denote the ground coverage of the Sentinel-1 images from different tracks (only two subswaths covering the epicenter areas are shown for each track). The red dashed line represents the approximate location of the Mountain Frontal Flexure, a topographic and structural relief step that divides the Zagros mountain range from its foreland to the southwest (Berberian, 1995; Emami et al., 2010). AR = Arabian plate; IN = Indian plate; EU = Eurasian plate; AF = Africa plate.

this event determined by the U.S. Geological Survey (USGS) is located ~50 km north of Sarpol-e Zahab city in Kermanshah province and only a few kilometers east of the Iran-Iraq border. Because of the sparse and uneven data reporting in Iran and Iraq, the USGS epicenter has a large uncertainty. Using data from local Iranian and Iraqi networks, Nissen et al. (2019) determined the epicenter of this event at 34.911°N, 45.800°E, a few kilometers north of Ezgeleh on the Iran-Iraq border, with a hypocentral depth of ~19 km. We refer to this event as the Sarpol-e Zahab (Iran) earthquake, given that Sarpol-e Zahab is the closest community with a sizeable population (over 30,000) and that most of the damage and fatalities were in this city. Focal mechanism solutions of this event indicate that this earthquake ruptured either a nearly north-south trending fault (i.e., NNW trending) that dips gently to the east, or a NW striking subvertical fault. Geological features around the 2017 Sarpol-e Zahab earthquake include an en echelon set of right-stepping approximately NW striking reverse faults and anticlines that are associated with shortening across a series of basement-involved blind faults, namely, the Mountain Frontal Fault (MFF) and the Zagros Foreland Fault (Berberian, 1995). Although the NW trending nodal plane roughly aligns with these features (Figure 1), its near-vertical dip angle makes this fault geometry unfavorably oriented in the overall compressional stress field and inconsistent with the wide distribution of aftershocks. Therefore, the more plausible east dipping rupture plane of the 2017 Sarpol-e Zahab earthquake does not closely align with the geologically mapped thrust faults in this region.

There have been several studies focusing on the source characteristics of this earthquake with both geodetic and seismic data (e.g., Barnhart et al., 2018; Chen et al., 2018; Feng et al., 2018; Gombert et al., 2019; Nissen et al., 2019). Although there are some variations among these published rupture models, they all show that

the 2017 Sarpol-e Zahab earthquake ruptured a nearly N-S trending fault with oblique thrust and dextral motion over a depth range of 12–20 km. In this study, we focus on the postseismic deformation during ~1 year after the mainshock. To ensure consistency, we first derive our own coseismic slip model for the mainshock using Sentinel-1 interferograms spanning the time of the mainshock. The results regarding the fault geometry and slip distribution are overall consistent with previously published studies. We next derive the postseismic deformation time series during the first year after the mainshock. Turbulent atmospheric delay in radar propagation is a significant error source in interferometric synthetic aperture radar (InSAR) time series analysis, which makes the measurement of low-amplitude ground motion, such as postseismic deformation, quite challenging. Previous studies using Sentinel-1 data of a similar time period concluded that the postseismic deformation months after the 2017 Sarpol-e Zahab earthquake was dominated by afterslip mainly updip of the coseismic rupture (Barnhart et al., 2018; Feng et al., 2018; Liu & Xu, 2019; Lv et al., 2020). In this study, we use the Common-Scene-Stacking (CSS) method (Tymofyeyeva & Fialko, 2015; Wang & Fialko, 2018) to mitigate the atmospheric noise. We show that after the atmospheric noise correction, postseismic line-of-sight (LOS) displacements derived from two Sentinel-1 ascending tracks show clear deformation both west and east of the coseismic slip contours. Both kinematic inversions and stress-driven afterslip simulations show that the observed postseismic deformation is well explained by aseismic afterslip both updip and downdip of the mainshock rupture. With the time series of postseismic InSAR measurements, we invert for the frictional properties of the fault updip and downdip of the 2017 Sarpol-e Zahab coseismic rupture, assuming that the afterslip is governed by a rate-strengthening friction law. We show that distinct frictional properties of updip and downdip of the coseismic rupture are required to explain the postseismic deformation after the 2017 Sarpol-e Zahab earthquake.

2. Data and Methods

2.1. InSAR Processing

Data used in this study include LOS displacements derived from synthetic aperture radar (SAR) data from four Sentinel-1 tracks (two ascending tracks ASC072 and ASC174 and two descending tracks DES6 and DES79, see Figure 1 for the respective scene coverages) of the Sentinel-1 A/B satellites. The SAR data are processed with GMTSAR (Sandwell et al., 2011). All images of the respective tracks are geometrically aligned to a master image using the orbital information and a Digital Elevation Model (DEM). To remove the occasionally appearing burst discontinuities that may be attributed to satellite clock errors and/or ionospheric effects, we further refine the image alignment with the Bivariate Enhanced Spectral Diversity (BESD) method (Wang et al., 2017). The topographic phase is removed using the 1 arc sec (i.e., 30 m) DEM derived from the Shuttle Radar Topography Mission (SRTM). The interferometric phase is unwrapped with SNAPHU (Chen & Zebker, 2001).

For the coseismic deformation, we form interferograms with image acquisitions that are closest in time to the mainshock, which include 5 to 7 days of postseismic deformation. The coseismic LOS displacements from four different view geometries are shown in Figure 2. Because of the arid and sparsely vegetated environment, the epicentral area exhibits high correlation of radar phase. LOS displacements from the two ascending tracks (ASC72 and ASC174) are characterized by mainly significant range decrease southwest of the USGS epicenter, while data from the descending tracks (DES6 and DES79) show range increase near the epicenter and range decrease further to the southwest. The difference in LOS deformation patterns of ascending and descending satellite tracks is indicative of significant horizontal motion.

To reduce the noise due to atmospheric perturbations and orbital inaccuracies, we flatten the LOS displacements of each track by removing a linear trend that depends on both local topography and coordinates:

$$\phi = a * x + b * y + c * h + d \tag{1}$$

where x and y are pixel coordinates along range and azimuth direction, respectively, and h is the elevation. We use pixels outside the expected earthquake deformation zone to estimate this trend. The resulting LOS displacements are then downsampled with a quad-tree curvature-based algorithm (e.g., Jónsson et al., 2002). To avoid oversampling in areas with large phase gradient due to noise (e.g., residual atmospheric noise and unwrapping errors), we perform the downsampling iteratively, using the current best-fitting model to generate the bounding coordinates of each quad-tree cell for the next iteration (Wang &
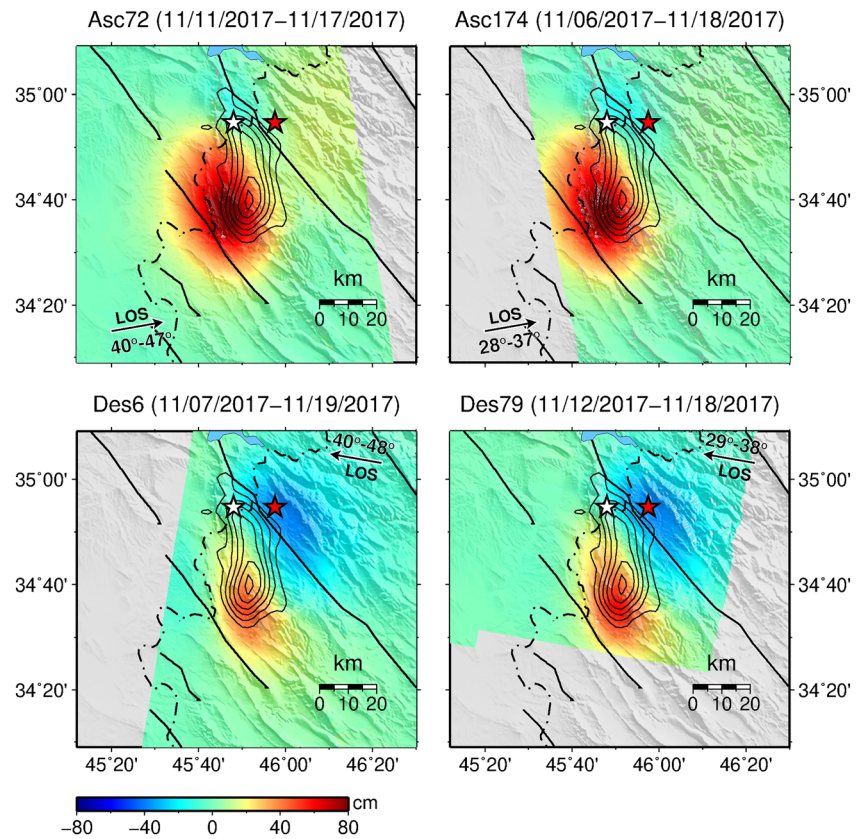
Figure 2. LOS coseismic displacements due to the 12 November 2017 Sarpol-e Zahab earthquake. Positive values correspond to surface motion toward the satellite. Red and white stars represent the epicenter of the *Mw* 7.3 mainshock determined by the U.S. Geological Survey and Nissen et al. (2019), respectively. Black lines denote the faults with dominantly thrust motion in this area. Arrows in each panel represents the LOS of each satellite track, and the numbers around the arrow denote the range of radar incident angle across the region shown on the map. Black contours denote the coseismic slip model derived in this study at 1-m intervals, starting at 1 m. Labels on top of each panel show the acquisition dates of the SAR images used to form the interferograms.

Fialko, 2015). For coseismic displacement, we estimate the data covariance by examining the spatial correlation of LOS displacements in the far field, where the range change variability is expected to be mostly from atmospheric noise. We assume that the atmospheric noise is spatially stationary and radially symmetric, so its spatial correlation depends only on the distances between observations. The resulting noise distribution function is then used to build the covariance matrix of the downsampled data points, assuming that the correlation between data points decays exponentially with distance (Sudhaus & Jónsson, 2009).

In response to the earthquake, the European Space Agency (ESA) amended the observation schedule to allow for data acquisitions along each track of Sentinel-1A and Sentinel-1B, leading to repeat intervals of 6 days for each satellite path over the epicentral area. By the end of January of 2019, there have been more than 70 postseismic acquisitions for all four tracks shown in Figure 1. To maintain a relatively high radar coherence, we limit the temporal baselines to be less than 50 days and the geometrical orbit baseline to be shorter than 200 m. We construct the time series of the postseismic deformation using the Small Baseline Subset (SBAS) method (e.g., Berardino & Fornaro, 2002; Schmidt & Bürgmann, 2003).

Noise due to atmospheric perturbations between image acquisitions is one of the major limitations in InSAR measurements of low-amplitude deformation, such as the postseismic transients. To reduce the atmospheric noise, in the analysis of postseismic deformation due to the 2017 Sarpol-e Zahab earthquake, we apply the method of CSS (Tymofyeyeva & Fialko, 2015). This method exploits the fact that interferograms sharing a common scene necessarily contain the same contribution of atmospheric delays from that acquisition.
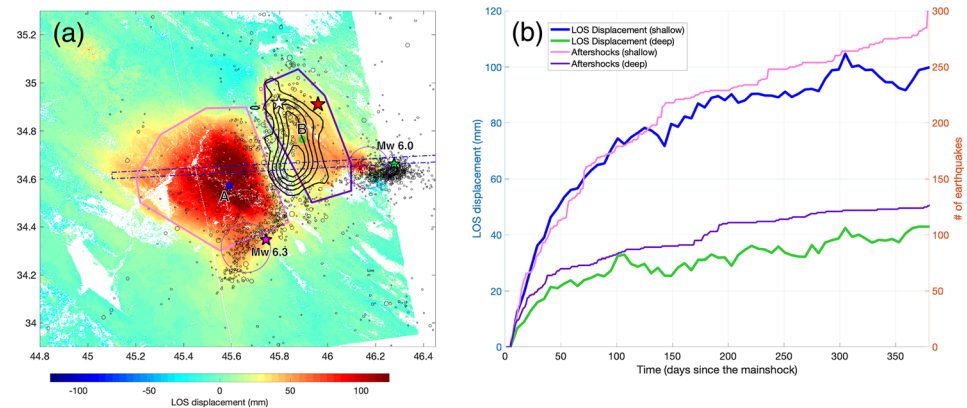
Figure 3. (a) Cumulative postseismic LOS displacement 1 year after the 2017 Iran-Iraq earthquake, derived from the Sentinel-1 data of the ascending track ASC72. Black circles represent the aftershocks of $M > 2.5$ during the same time-period from Iranian Seismological Center (http://irsc.ut.ac.ir/). Green and magenta stars denote the epicenters of the two largest aftershocks on 25 August and 25 November 2018, respectively. Polygons in pink and purple represent the areas for which the aftershock temporal evolutions are shown in (b). Dashed purple circles outline the areas within which the LOS displacements are not used in the afterslip modeling. (b) Temporal evolution of postseismic deformation and cumulative number of aftershocks updip and downdip of the mainshock rupture. Blue and green curves represent the postseismic LOS displacements at Points A (updip) and B (downdip), respectively. Magenta and yellow curves represent the cumulative numbers of aftershocks within the updip and downdip polygons in (a). We correct for the atmospheric noise with Common-Scene-Stacking (Tymofyeyeva & Fialko, 2015). No temporal evolution function or smoothing is applied when solving for the postseismic deformation time series.

Therefore, by stacking many interferograms that share a common scene, one can estimate the atmospheric phase screen (APS) of that scene, assuming that the atmospheric noise is random in time and that the tectonic deformation cancels out or can be roughly corrected for. Details of the method can be found in Tymofyeyeva and Fialko (2015) and Wang and Fialko (2018). In order to maintain the temporal resolution in the final deformation time series, we limit the stacking stencil to be no greater than 18 days on each side of the target scene, resulting in a maximum of six interferograms per stack in the case of 6 days repeat intervals. We note that the CSS method is intrinsically similar to low-pass filtering that is often adopted to suppress atmospheric noise for InSAR time series analysis (e.g., Ferretti et al., 2000; Hooper et al., 2007); however, it has a few advantages. First, the stacking is carried out in an order determined by the noise level of all images. APS of images with higher noise levels are estimated first, which are then used to correct the pertinent interferograms before proceeding to the next scene. This reduces the possible leakage of noise from very "bad" scenes to more quiet ones. Second, the stacking is performed on the entire image, so it is computationally quite efficient. Lastly, this method can easily deal with cases of irregular acquisition intervals, for example, missing data in the stack.

Postseismic LOS displacement time series derived from data along the Ascending Track ASC72, with and without correction of atmospheric noise with CSS, are shown in Figures S1 and S2 in the supporting information, respectively. While both time series exhibit significant range decrease (i.e., movement toward the satellite) over much of the image, the results with atmospheric correction are much more coherent in time. In particular, in addition to the major zone of range decrease southwest of the coseismic rupture (i.e., updip of the coseismic rupture), a narrow band of temporally coherent range decrease is also evident east of the mainshock epicenter, with partial overlapping with the surface projection of the coseismic rupture (Figure S2). This feature, however, is not clear in the results without atmospheric correction (Figure S1). The cumulative LOS displacements for the Ascending Track ASC72 1 year after the 2017 Mw 7.3 Sarpol-e Zahab mainshock and the corresponding time series at two selected points are shown in Figures 3a and 3b, respectively.

The cumulative postseismic LOS displacements along all four satellite tracks are shown in Figure 4. LOS displacements of the two ascending tracks (ASC72 and ASC174) are characterized by two separate zones of significant range decrease southwest and east of the coseismic rupture (black contours in Figure 4). In particular, the range decrease west of the coseismic rupture is distributed across a wide area, with a
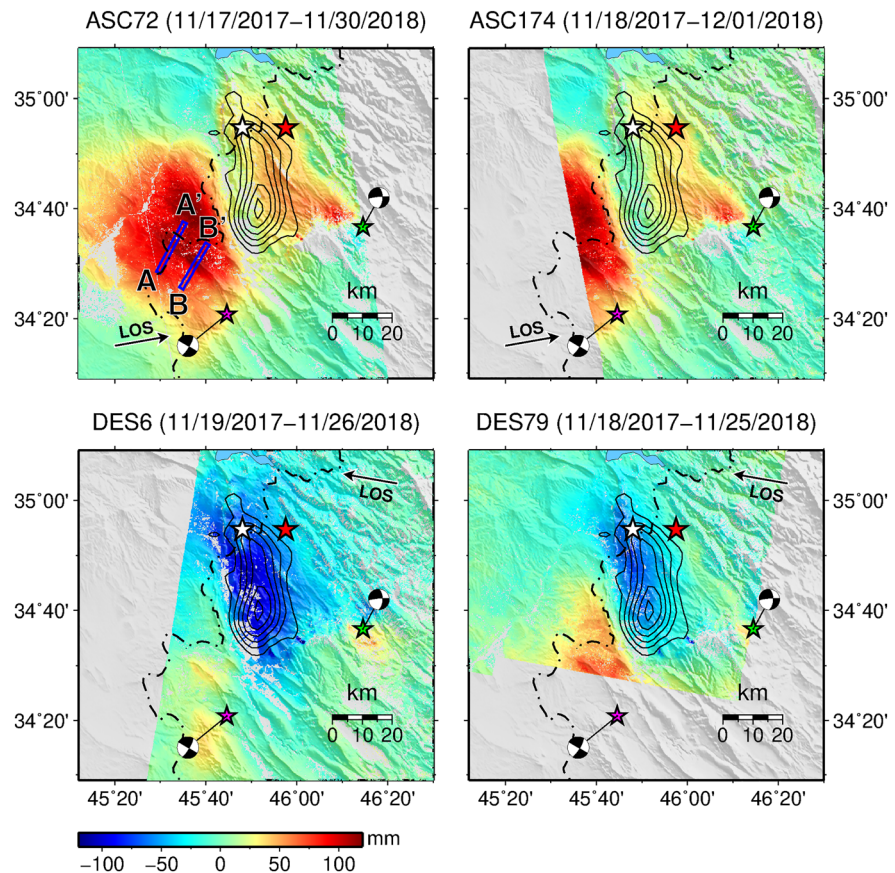
Figure 4. Cumulative postseismic LOS displacements from four Sentinel-1 tracks. Dates of first and last image acquisitions used are shown on top of each panel. Since CSS has poorer performance in correcting for atmospheric noise of images at the two ends of the catalog, we discarded the last few scenes to determine the postseismic deformation, although the processed data extend until the end of January 2019. Red, green, and magenta stars represent USGS epicenters of the Sarpol-e Zahab *Mw* 7.2 mainshock on 12 November 2017, the *Mw* 6.0 aftershock on 25 August 2018, and the *Mw* 6.3 aftershock on 25 November 2018, respectively. Blue boxes in the top left panel show the profile locations for which the LOS displacement time series are shown in Figure 11. Note that the first postseismic image of all four satellite tracks was acquired about 5 days after the mainshock and within less than 2 days of one another.

maximum value exceeding 10 cm during 1 year after the mainshock. LOS displacements of the two descending tracks (DES6 and DES79), on the other side, are characterized by an elongated zone of range increase primarily right above the coseismic rupture, plus some relatively localized range decrease southwest of the coseismic rupture. Similar to the coseismic deformation field, the different patterns of LOS displacements between ascending and descending satellite tracks indicate that postseismic relaxation of the 2017 Sarpol-e Zahab contains significant horizontal motion.

2.2. Modeling of Coseismic Deformation

In this section, we invert the coseismic surface deformation data for the geometry and distribution of slip of the rupture. In our modeling, we calculate Green's function relating a unit slip to surface displacement using the solution of a rectangular dislocation in a homogeneous elastic half-space with a Poisson's ratio $\nu = 0.25$ (Okada, 1985). Fault geometry, including the fault position, strike, dip, and rake angles, is nonlinear parameters in the coseismic slip inversion. Thus, they are often not well constrained when the data quality and/or quantity are limited, leading to a potential bias in the resulting slip distribution. To mitigate this limitation, here we first invert for the fault geometry of the 2017 Sarpol-e Zahab earthquake assuming a single rectangular fault patch. Model parameters in this inversion include the location of the fault centroid (eastward and northward shift (x, y) with respect to the epicenter of the earthquake) and depth, length, width, strike, dip and rake, and slip magnitude of the dislocation. To quantify the uncertainty of the
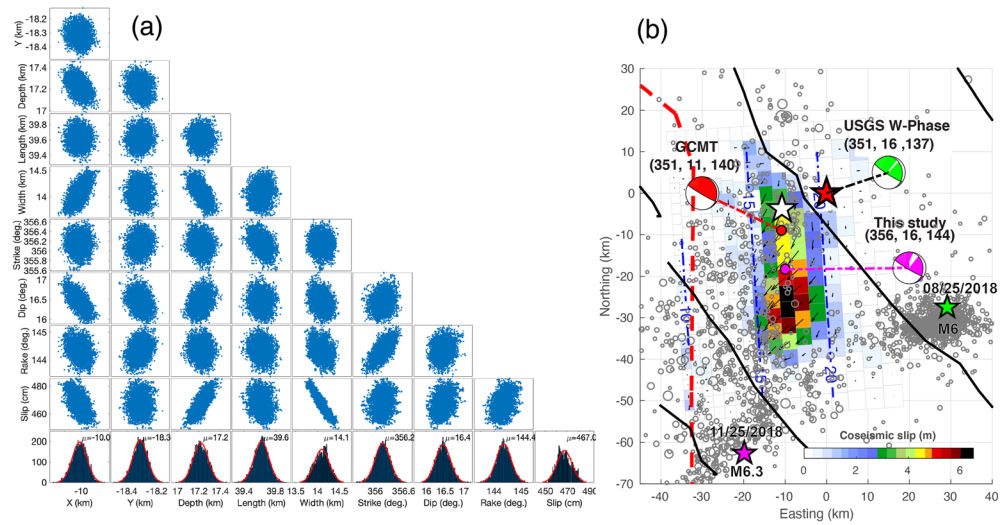
Figure 5. Inversion of fault geometry and slip distribution of the 2017 Sarpol-e Zahab earthquake. (a) Distribution of model parameters in the inversion for fault geometry assuming a single rectangular slip patch. Locations (eastward *X*, northward *Y*, and depth) represent the center of the rectangular dislocation with respect to the USGS epicenter at 34.911°N, 45.959°E. (b) Coseismic slip model of the 2017 Sarpol-e Zahab earthquake. Gray circles denote the aftershocks of *M* > 3 till 3 December 2018 from the Iranian Seismic Center (ISC) (http://irsc.ut.ac.ir/). Numbers above beach balls represent the strike, dip, and rake angles of the rupture. Dashed blue lines represent depth contours of the fault plane in km, and the red dashed line is the approximate location of the Mountain Frontal Flexure (see Figure 1).

model parameters, we implement the inversion in a Bayesian inversion framework. We assume a uniform prior distribution within a wide range for each model parameter and a Gaussian distribution for the observation errors. We sample the model space with a *slice* sampling algorithm in Matlab (Neal, 2003).

The distribution of the model parameters that yield a comparatively high posterior probability density function (PDF) is shown in Figure 5a. Thanks to the nice coverage of InSAR observations from different look directions, most of the model parameters are tightly constrained. However, we note that the acceptable range of model parameters depends on the error functions of the input data, which we estimate using data outside the deformation area with simplified assumptions that the atmospheric noise is spatially homogeneous, isotropic, and exponentially decays with distance. The results show that the 2017 Sarpol-e Zahab earthquake rupture can be approximated by an almost north-south trending (strike = 356°) fault plane that is 40 km long and 15 km wide and gently dips to the east (dip angle = 17°), with an average slip of ~467 cm and rake angle of 144°. The slip centroid is found to be at a depth of ~17 km located ~20 km southwest of the USGS epicenter. As expected, there is some trade-off between the slip magnitude and fault dimension, particularly with the fault width, and depth. A moderate trade-off also exists between the strike and rake angles. Nevertheless, all models yielding a high posterior PDF have a northerly strike angle. In particular, models with a strike angle that aligns with the overall structural trend in this area (~330°) fail to correctly predict the range increase (corresponding to subsidence if there is no horizontal motion) north of the major lobe of range decrease (uplift) observed in the two ascending tracks (ASC72 and ASC174), regardless of the other parameters. The preferred strike angle of 356° is 20–30° from the average strike of surface expressions (i.e., folding and previously mapped faults) of this area (Figure 1). The preferred strike of the 2017 Sarpol-e Zahab rupture, however, is similar to the overall orientation of the Mountain Frontal Flexure (Figure 1), a structural and topographic front that separates the high Lurestan arc to the east from the low Kirkuk embayment to the west near the epicentral area (Berberian, 1995). The preferred fault geometry and slip direction are in good agreement with the W-phase focal mechanism determined by USGS and the moment tensor solution by gCMT (Figure 5b). Overall, surface displacements predicted by the preferred model of a single dislocation patch match the observations well (Figure S3).

We next examine the detailed slip distribution of the 2017 *Mw* 7.3 Sarpol-e Zahab earthquake based on the fault geometry that is determined from the single dislocation inversion above. The ~70-km-long by 55-km-wide fault plane is divided into patches whose size gradually increases along the downdip

direction to ensure a relatively uniform model resolution. Each individual patch is allowed to have a thrust and right-lateral slip component of up to 10 m. Laplacian smoothing is applied between adjacent fault patches to avoid abrupt variations in slip. We further regularize the inversion problem by requiring no slip at the fault edges, except at the updip edge of the fault. The optimal value of the smoothness is chosen by visual inspection, such that the resulting slip model appears smooth enough without significantly deteriorating the data fitting.

Our preferred coseismic slip model of the mainshock is shown in Figure 5b. Similar to the model of a single dislocation patch, the model allowing for spatial variation in slip is also characterized by oblique slip, with nearly equal amounts of dextral and thrust components. The distributed slip model, however, has somewhat larger slip in the southern half of the rupture. The area of prominent slip (>1 m) is ~40 km long by ~17 km wide, similar to the dimension of the preferred model of the single dislocation patch. The majority of the moment release is confined in a depth range between 15 and 20 km, with a maximum slip of ~6.5 m at a depth of ~17 km, well beneath the estimated 6- to 10-km thickness of sedimentary cover in the Lurestan arc (Emami et al., 2010; McQuarrie, 2004; Vergés et al., 2011). The bottom of the coseismic slip model closely aligns with the base of the seismogenic zone in this region (Karasözen et al., 2019). Assuming a shear modulus of 30 GPa, the total moment release is estimated to be ~8.9×10^{20} Nm, corresponding to a moment magnitude of 7.26, which is in good agreement with the seismic moment. The preferred slip model predicts surface displacements that fit the observations well (Figure S4). Compared to the result with a single patch, the model with variable slip distribution yields overall better fitting to the observations, particularly in the area south of the moment centroid, where the estimated slip is larger than average. The preferred coseismic slip model shown in Figure 5b is overall consistent with previous studies (e.g., Barnhart et al., 2018; Feng et al., 2018; Nissen et al., 2019; Vajedian et al., 2018).

3. Modeling of Postseismic Deformation

Commonly considered models of postseismic deformation include afterslip, poroelastic rebound, and viscoelastic relaxation. Viscoelastic relaxation takes place mainly in the lower crust and/or upper mantle, where the temperature and pressure are high enough to allow for ductile flow of rocks (Bürgmann & Dresen, 2008). The observed large surface deformation updip of the coseismic rupture indicates that the deformation source is relatively shallow, and thus unlikely to be due to viscoelastic relaxation. Published models also suggest that postseismic deformation due to deeper seated viscoelastic relaxation 1 year after 2017 Sarpol-e Zahab earthquake is small (< ~3 mm), even when choosing rather low viscosities in the lower crust and upper mantle (e.g., Barnhart et al., 2018). We show in the supporting information that the contribution from poroelastic rebound is also negligible (<5 mm), although the magnitude and spatial pattern of surface deformation depend on the hydraulic properties of the host rocks (i.e., porosity and hydraulic diffusivity) (Figures S5 and S6). In the next section we show that the observed postseismic deformation ~12 months after the 2017 Sarpol-e Zahab is well explained by afterslip both updip and downdip of the coseismic rupture. In addition to dominantly aseismic afterslip, large aftershocks contribute to the observed cumulative postseismic deformation. On 25 August 2018, a *Mw* 6.0 aftershock occurred ~30 km southeast of the mainshock (https://earthquake.usgs.gov/earthquakes/eventpage/us1000ghda/executive). Three months later on 25 November 2018, another strong aftershock of *Mw* 6.3 occurred near the southern edge of the updip deformation zone but at ~20-km depth (https://earthquake.usgs.gov/earthquakes/eventpage/us1000hwdw/executive). Both events produced ~2- to 3-cm-range changes around the respective epicenters in the cumulative postseismic deformation field (Figure 3 and 4). Focal mechanism solutions of these two aftershocks are both characterized by strike slip along nearly vertical nodal planes. The contrasting depths, rupture orientations, and dip angles show that these two large aftershocks occurred on structures different from the mainshock and afterslip fault planes. To avoid a potential bias in the study of postseismic deformation processes, we mask out pixels around the epicenters of these two largest aftershocks.

3.1. Kinematic Inversion of Afterslip

Assuming that the observed postseismic deformation is purely due to afterslip, we optimize the geometry of the fault updip of the coseismic slip and invert for the spatial distribution of afterslip. The cumulative LOS displacements on all four tracks shown in Figure 4 are used in the inversion. Our inversion of the afterslip distribution is based on the fault geometry that was derived from the modeling of coseismic deformation,
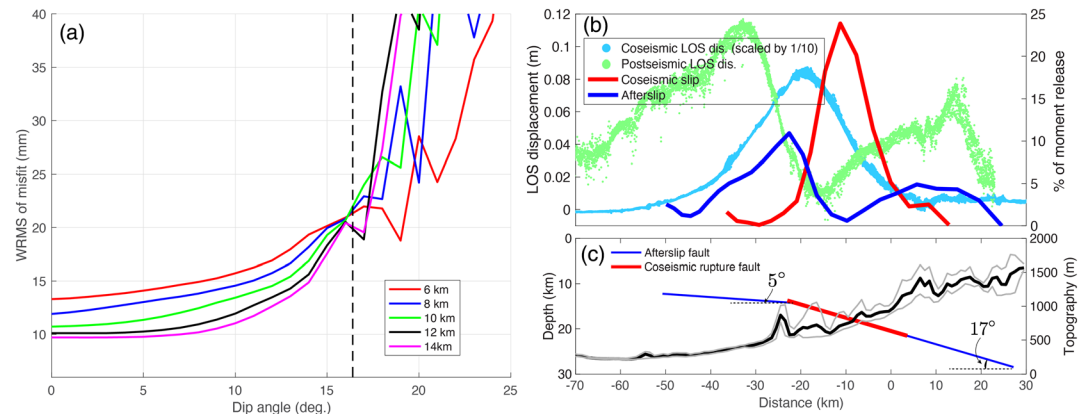
Figure 6. Optimization of updip fault geometry and comparison of surface displacements due to coseismic rupture and afterslip. (a) Root-mean-square (RMS) of data misfit as a function of dip angle of the shallow afterslip fault plane in the inversion of afterslip. Colors represent different "transition" depths above which the dip angle is allowed to vary from that of the coseismic rupture. The dip angle below the "transition" depth is fixed at 17° (dashed line). (b) LOS displacements of the ascending track ASC72 (light blue: coseismic/10 and green: postseismic) and percentage of moment release due to coseismic slip (red) and afterslip (blue) along a profile perpendicular to the coseismic rupture. (c) Cross section of fault geometry for coseismic rupture and afterslip. Red and blue lines delineate the coseismic and afterslip segments, respectively.

with extensions in both strike and dip directions. To account for a possible variation in fault geometry associated with a ramp-and-flat system at the mountain front, the dip angle is allowed to vary above a certain depth (hereafter called the "transition" depth). The dip angle beneath this transition depth is held fixed at 17° found in the coseismic modeling, while the dip angle above the transition depth is a free parameter in the inversion. We varied the transition depth from 6 to 14 km at 2-km intervals. For each configuration of fault geometry, we then invert for the afterslip distribution and examine the corresponding data fitting by computing the root-mean-square (RMS) of the residual between model and observation, which is defined as $\text{RMS} = \sqrt{\dfrac{(d - d')^2}{N}}$, where d represents the vector of downsampled InSAR LOS displacements, the vector of d' model predictions, and N the number of observations.

Figure 6a shows the RMS of the model misfit as a function of dip angle for the shallow afterslip fault plane. One clear feature is that for all the explored transition depths, the data fitting deteriorates with an increasing dip angle of the shallow part of the fault. This suggests that the dip angle of the shallow afterslip is smaller than that of the mainshock rupture plane of 17°. However, models with dip angle smaller than 10° updip of the transition depth yield similar data misfit, suggesting that the data have little resolution for the dip angle smaller than 10°. We therefore take a value of 5° as the dip angle for the updip afterslip fault plane. We did a similar test for the dip angle downdip of the coseismic rupture and found that a wide range of dip angles (0–25°) can fit the data equally well, indicating that the data do not have sufficient sensitivity to resolve the downdip fault geometry. We therefore propose a kinked fault geometry as shown in Figure 6c, which has a dip angle of 5° above ~10–14 km and 17° beneath. We note that the transition depth determined in this study may have large uncertainties due to the limited data resolution. The preferred fault geometry is overall consistent with geological cross sections across the Zagros, which feature a subhorizontal detachment at a depth of ~6–10 km that separates the Phanerozoic sediments from the underlying crystalline basement (e.g., Emami et al., 2010; McQuarrie, 2004; Vergés et al., 2011).

We then invert for the distribution of cumulative afterslip using postseismic InSAR observations from all four satellite tracks observed from 5 days after the mainshock to November 2018 (Figure 4). The preferred distribution of afterslip based on this geometry is shown in Figure 7a. Similar to the coseismic slip model, the afterslip model is characterized by oblique slip containing nearly equal components of thrust and dextral motion, with distinct slip zones located both updip and downdip of the coseismic rupture. Little or no afterslip is found in the area of high coseismic slip, despite the spatial smoothing. The maximum slip updip of the coseismic rupture exceeds 0.8 m during the observation period (from a few days after the mainshock to the
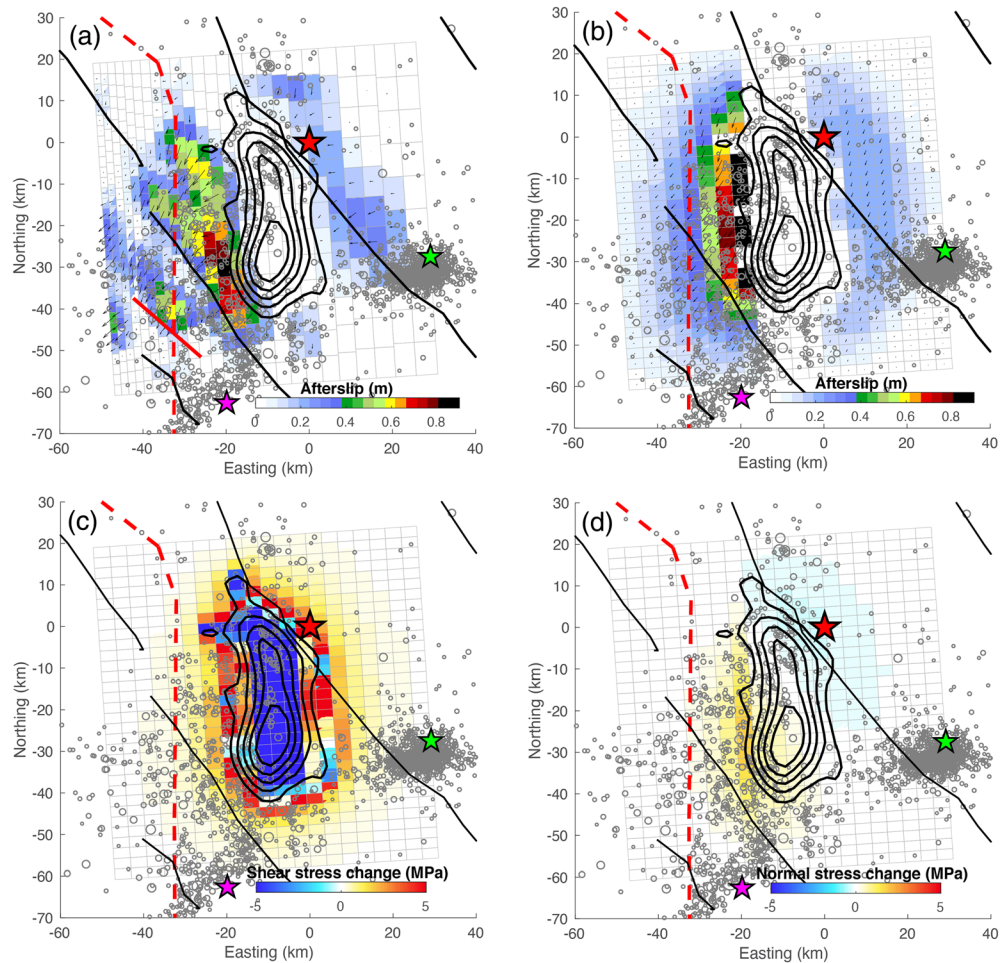
Figure 7. Afterslip models from (a) kinematic inversion of postseismic deformation and (b) stress-driven afterslip simulation assuming a rate-strengthening fault friction. Note that because the first postseismic SAR image was acquired on 17 November 2017, both models shown here do not include afterslip during the first 5 days after the mainshock. Panels (c) and (d) show the shear (along the coseismic slip direction) and normal stress changes (positive for unclamping) produced by the coseismic rupture, respectively. Yellow circles represent $m > 2.5$ aftershocks (from ISC catalog) during the InSAR observation period. Red, green, and magenta stars denote the USGS epicenters of the Mw 7.3 mainshock on 12 November 2017, the Mw 6.0 aftershock on 25 August 2018, and the Mw 6.3 aftershock on 25 November 2018, respectively. Solid red line in (a) denotes the surface trace across which both coseismic and postseismic deformation exhibit sharp offsets (Figure 10).

end of November 2018). The inferred peak slip in the downdip afterslip zone is ~0.3 m. The cumulative moment due to afterslip is 2.3×10^{19} Nm, which amounts to ~20% of the coseismic moment release and is equivalent to the moment of a Mw 6.84 earthquake. About 75% of the moment release occurred on the updip section of the coseismic rupture. The moment release calculated from the inferred afterslip model is significantly higher than the aftershocks during this time period, which add up to 3.03×10^{17} Nm and 3.08×10^{16} Nm for the updip and downdip regions (delineated by pink and purple polygons in Figure 3a), respectively. This indicates that the postseismic deformation of the 2017 Sarpol-e Zahab earthquake is dominated by aseismic afterslip, which has also been observed for many other events (e.g., Bürgmann et al., 2002; Hsu et al., 2006; Perfettini et al., 2010). Nonetheless, aftershocks may locally contribute more to accommodate the postseismic fault slip, compared to aseismic afterslip, which is often poorly resolved in geodetic afterslip models because of the spatial smoothing and/or other numerical regularizations involved in the inversions (Lange et al., 2014). Surface deformation predicted by the afterslip model shown in Figure 7a matches the observations well, except in the area close to the Mw 6.0 aftershock on 25 August 2018 (marked as green stars in Figures 3 and 4), where the relatively large residuals likely result from the deformation associated with this event, which is not considered in our modeling (Figure 8).
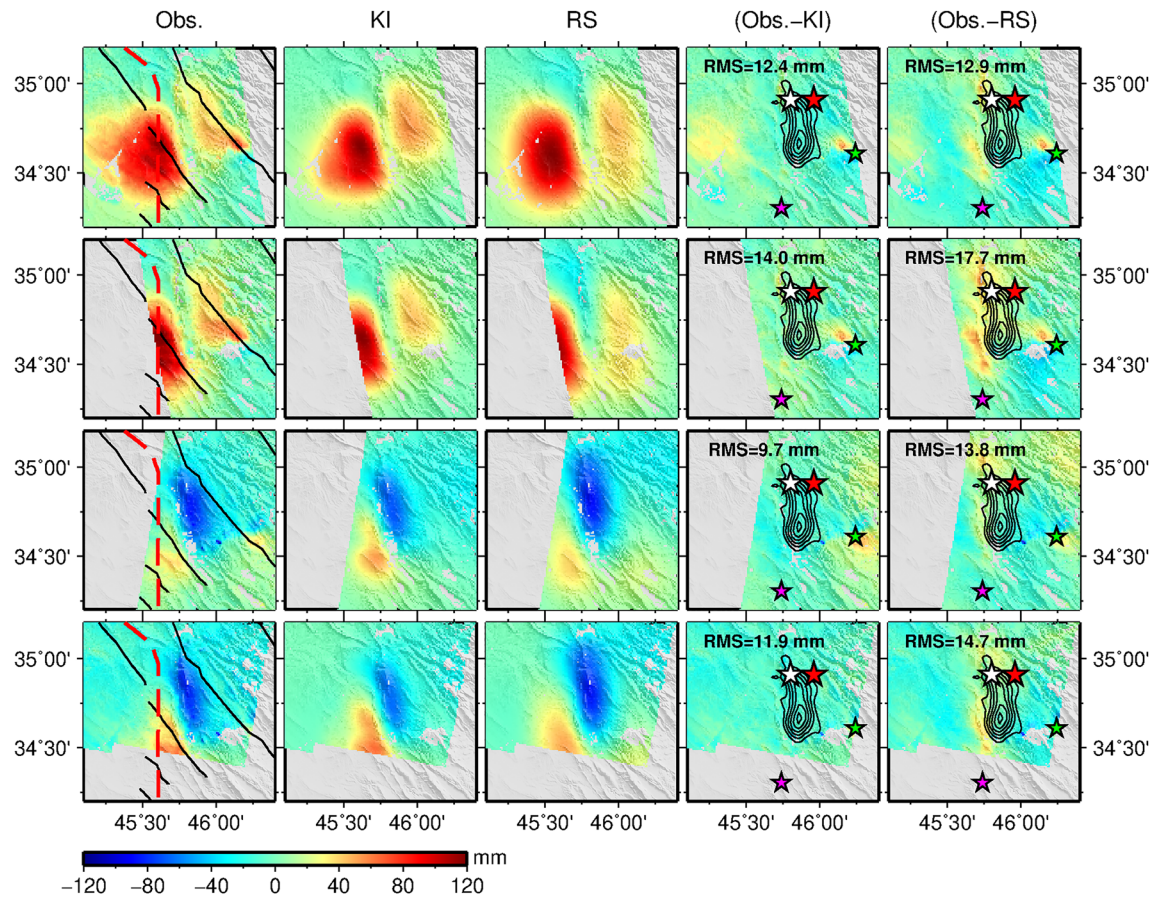
Figure 8. Comparison of cumulative surface displacements between observations and the kinematic inversion (KI) and rate-strengthening (RS) model predictions. Observation periods for each track are the same as shown in Figure 4. Red, green, and magenta stars in the last two columns denote the USGS epicenters of the *Mw* 7.3 mainshock, the *Mw* 6.0 aftershock on 25 August 2018, and the *Mw* 6.3 aftershock on 25 November 2018, respectively. Numbers in the last columns show the RMS of misfit at downsampled data points.

3.2. Stress-Driven Afterslip Simulation

The kinematic inversions indicate that the observed postseismic deformation 1 year after the 2017 Sarpol-e Zahab earthquake is well explained by afterslip both updip and downdip of the coseismic rupture. To verify whether such an afterslip model is consistent with stress changes induced by the coseismic rupture and to explore the frictional properties of the fault, we model the afterslip assuming that the evolution of afterslip is governed by rate-and-state friction (e.g., Marone, 1998; Ruina, 1983). Rather than using the full rate-and-state equations, we assume a steady-state rate-strengthening friction without healing and slip-weakening effects. The simulation of afterslip with rate-strengthening and full rate-and-state constitutive laws only differs in the very early stage of the postseismic phase, when the cumulative afterslip is less than the critical slip distance over which the state variable evolves (Barbot et al., 2009; Marone, 1998; Perfettini & Avouac, 2007). The postseismic InSAR observations in this study started 5–7 days after the mainshock, during which the cumulative afterslip is expected to already have greatly exceeded the critical slip distance D_c in the full rate-and-state frictional law. The rate-strengthening simplification is also supported by the high-sampling-rate GPS observations shortly after the 2016 Kumamoto earthquake (Milliner et al., 2020). Under the rate-strengthening simplification, the fault slip rate at the onset of the afterslip can be expressed as (e.g., Barbot et al., 2009) follows:

$$V = 2V_0 \sinh \frac{\Delta \tau}{a\sigma} \tag{2}$$

where V_0 is a reference slip rate before the coseismic shear stress change $\Delta\tau$ is applied, σ is the effective normal stress on the fault, and a is a constitutive parameter representing the dependence of friction on the slip rate change. We that $a\sigma$ in Equation 2 should be interpreted as $(a - b)\sigma$ in the case of full rate-and-state friction. Here we have assumed that the normal stress change on the fault during an earthquake is small and negligible, compared to the shear stress change (Figures 7c and 7d). We note that V_0 does not correspond to the interseismic loading rate (Barbot et al., 2009; Perfettini & Avouac, 2007), as the nucleation process and propagation of dynamic waves during the rupture process may accelerate the creep rate in the afterslip zone, leading to a significantly larger V_0 compared to the long-term interseismic loading rate V_{pl} (Perfettini & Avouac, 2007).

A fault of the same geometry as in the kinematic afterslip inversion is discretized into rectangular patches of uniform size of ~4 by 3 km. The coseismic slip model shown in Figure 5b is used to generate the coseismic stress change in a uniform elastic half-space. In the depth range between 15 and 20 km, where most of the coseismic slip occurs, the shear stress change is negative (i.e., represents the stress drop). To avoid back slip, the afterslip on fault patches of coseismic slip >0.5 m is prescribed to be 0 and afterslip is only allowed to occur on patches whose centroid depths are smaller than 15 km (updip region) or larger than 20 km (downdip region). This is also consistent with the kinematic afterslip inversion results, which suggest that most afterslip occurs either updip or downdip of the coseismic rupture, with little, if any slip in the depth range of the coseismic rupture. This parameterization also implies that the fault segments laterally adjacent to the coseismic rupture are "locked" and are not allowed to participate in the afterslip. The rake of slip on each fault patch is determined by the direction of shear traction on the corresponding patch in each step.

Informed by the observation that the surface deformation and seismicity downdip of the coseismic rupture seem to decay faster than the updip region (Figure 3b), we allow for different frictional properties updip and downdip of the coseismic rupture. The model thus includes four free parameters: V_0 and $a\sigma$ for both the updip and downdip regions. We perform the numerical simulations with Unicyle (Barbot et al., 2017) We treat the simulation as an inverse problem, that is, given the surface deformation data, we solve for the parameters that can best explain the data.

Different from the kinematic afterslip inversion, in which only the cumulative surface deformation is used (Figure 4), here we use the time series of postseismic LOS displacements from the two ascending tracks ASC72 and ASC174, which have an overall better signal-to-noise ratio, and exhibit clear separation of surface deformation updip and downdip of the coseismic rupture. Figures 8, 10 and S8–S10 show that the preferred model is able to predict surface deformation of all four satellite tracks reasonably well. We uniformly downsample the InSAR LOS displacements at each postseismic epoch, and discard the data with total cumulative displacements of less than 3 cm. Since the InSAR time series are referenced to the first image acquisitions 5–6 days after the mainshock, the model predicted displacement at the starting epoch is subtracted from the time series of each track. The observed time series are compared with the model predictions to draw inferences about the frictional properties of the fault that minimize the misfit. We solve the problem in a Bayesian inversion framework, assuming that data are uncorrelated in space with a uniform standard deviation of 2 cm and that all four model parameters have uniform a priori distributions. Similar to the coseismic slip inversion, we sample the model space using a slice sampling algorithm (Neal, 2003).

The evolution of model parameters during the Bayesian inversion is shown in Figure 9. We note that all four parameters converge after ~200 samples, and the converged values do not depend on the initial values. We note that the "samples" shown here are only results with posterior likelihood improvement in the slice sampling.

The models yielding low data misfit have distinct values of V_0 and $a\sigma$ for updip and downdip portions of the fault; however, there is a strong trade-off between V_0 and $a\sigma$ (Figures 9c and 9f). For updip region, mean values of $a\sigma$ and V_0 favored by the data are 2.7 MPa and 1.42 m/year, respectively, in significant contrast to 0.073 MPa and 0.06 m/year for the downdip region. As the value of $a\sigma$ is the product of the dependence of friction on sliding velocity a, which is a constitutive property of the fault zone, and the effective normal stress σ, the large contrast in updip and downdip of the coseismic rupture indicates that either the rock properties or effective normal stress or both in these regions are different. In section 4 below, we briefly discuss the possible cause of such distinct frictional properties at those depth ranges.
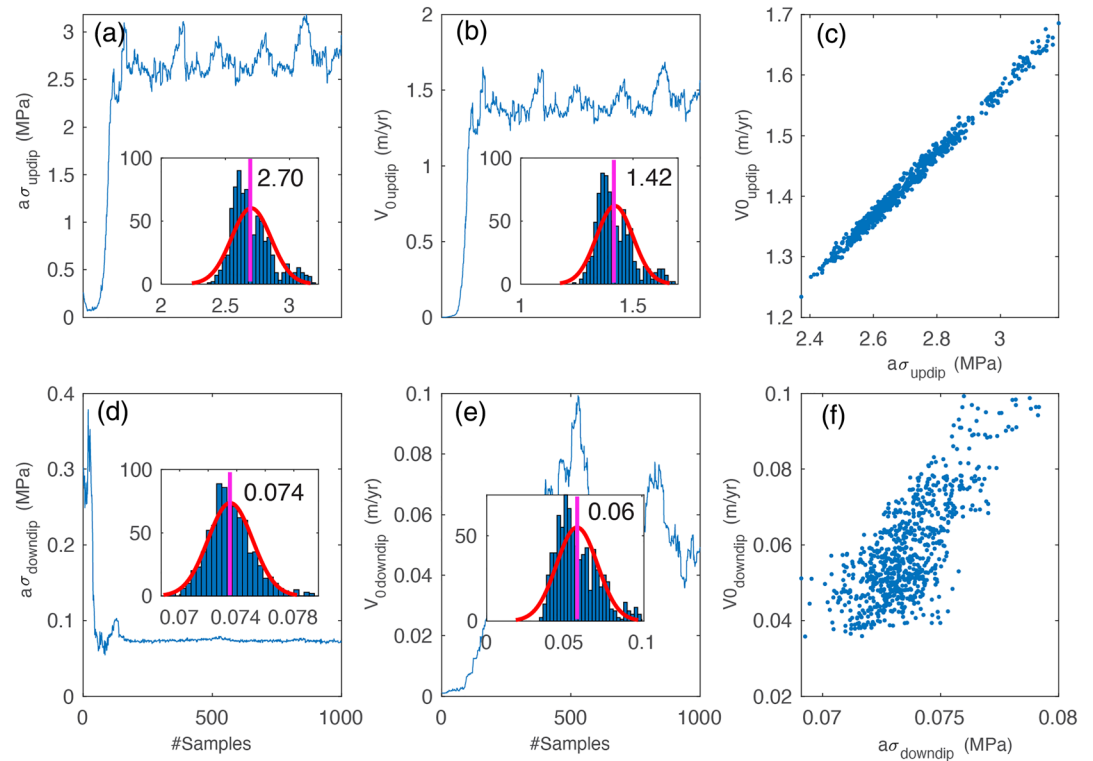
Figure 9. Sampling histories and distributions of model parameters in the afterslip simulation for fault patches updip (a and b) and downdip (d and e) of the coseismic rupture. The correlation between V_0 and $a\sigma$ are shown in (c) and (f). Insets in each panel show the histogram of the corresponding parameter after 200 burn-in samples. Red curves represent the best fitting normal distributions of samples after burn-in and are labeled with their mean values.

To test if such a large difference in frictional properties is resolvable by our dataset and the inversion procedures, we run a sensitivity test. We first generate the synthetic InSAR time series using the same rate-strengthening model with $V_0 = 1.5$ m/year and $a\sigma = 1.5$ MPa for the updip part of the fault and $V_0 = 0.01$ m/year and $a\sigma = 0.15$ MPa for the downdip part of the fault. These values produce distinct magnitudes and temporal evolutions of surface displacements updip and downdip of the coseismic rupture, similar to the observations. Gaussian noise with a standard deviation of 2 cm is added to the synthetic time series. We then invert for the model parameters: V_0 and $a\sigma$ for fault sections updip and downdip of the coseismic rupture. The results are shown in Figure S7. Similar to the inversion with real data, all four parameters converge to their respective values after ~200 iterations. The preferred values of parameters updip of the coseismic rupture, however, are slightly higher than the input ones. This is likely due to the fact that for each point we have shifted the synthetic time series (with noise) by the displacement of its first epoch, to mimic the real InSAR time series. The high degree of recovery revealed by this test indicates that with current data distribution, noise characteristics, and inversion procedures, it is possible to differentiate the frictional parameters updip and downdip of the coseismic rupture.

The model with the preferred values for $a\sigma$ and V_0 shown in Figure 9 produces surface deformation matching the observations well, both in time and space (Figure 8). The comparison of cumulative and time series of surface deformation between observations and model predictions for the ascending track ASC72 is shown in Figure 10. The residuals between observations and model predictions are generally less than 3 cm, comparable to the InSAR noise. Besides the major deformation zones of range decrease, the model also predicts a modest range increase in an area close to the northern tip of the coseismic rupture. This feature, however, is not clear in the data. In fact, range increase or surface subsidence at the northern tip of the fault is somewhat expected, because similar to the coseismic rupture, afterslip of the 2017 Sarpol-e Zahab earthquake is also characterized by a strong component of right-lateral strike slip, which exerts "pull" to the material north of the slip area to produce subsidence at the northern end of the coseismic rupture. Alternatively, the
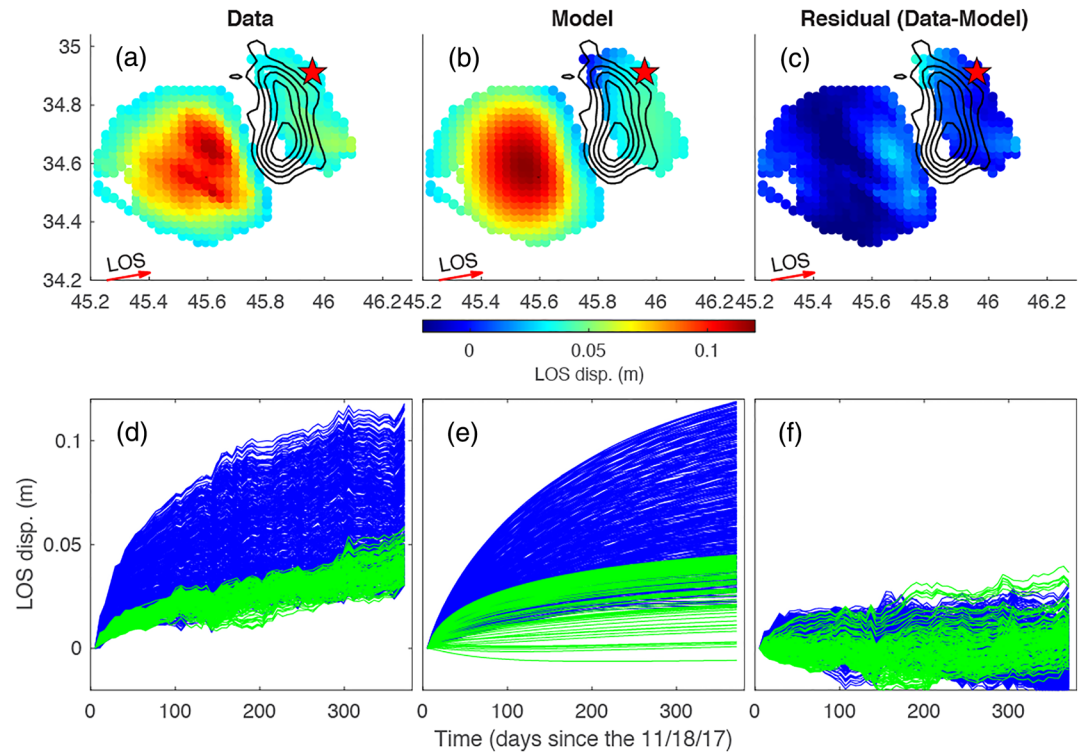
Figure 10. Comparison of surface deformation between observations and model predictions for the Ascending Track ASC72. (a–c) Cumulative LOS displacements larger than 3 cm after downsampling. Red star denotes the epicenter of the mainshock. (d) Observed, (e) modeled, and (f) residual time series of LOS displacements at all downsampled points. Gray and red curves represent the time series at locations updip and downdip of the coseismic rupture, respectively.

difference between model and observations in this area could be attributed to the simplified model assumption in our simulation. Our model does not allow for along-strike variation in the frictional properties and assumes a rate-weakening rheology over the depth range of major coseismic slip (15–20 km) to prevent any slip on fault patches on and adjacent to the rupture. In reality, some degree of afterslip may take place at the two along-strike ends of the coseismic asperity, as suggested by the kinematic afterslip inversion (Figure 7a). The model also predicts surface deformation that matches the observations of the other three InSAR tracks reasonably well (Figures 9 and S8–S10).

The cumulative afterslip predicted by the best fitting rate-strengthening afterslip model during the InSAR observation period (from 17 November 2017 to the end of November 2018) is shown in Figure 7b. Both the slip distribution and magnitude of the stress-driven afterslip model is very similar to that based on kinematic afterslip inversion. On the other hand, both the kinematic inversion and rate-strengthening afterslip models show significantly higher afterslip updip of the coseismic rupture, compared to the afterslip downdip of the coseismic rupture, although coseismic stress changes updip and downdip of the coseismic rupture are very similar (Figure 7c and 7d). This suggests that postseismic deformation during ~1 year following the 2017 Sarpol-e Zahab earthquake is indeed dominantly controlled by afterslip driven by the coseismic stress change; however, the frictional properties updip and downdip of the coseismic rupture are quite distinct. Our rate-strengthening afterslip model suggests that until the end of the InSAR observation period of this study, afterslip has released 76% and 93% of its total potential moment for regions updip and downdip of the coseismic rupture, respectively, assuming that the coseismic stress change will eventually be fully relaxed via afterslip. The model also suggests that during the period between the mainshock on 12 November 2017 and the first SAR image acquisition on 17 November 2017, moment release from early afterslip updip of the coseismic rupture is ~3% of its total moment after full relaxation, whereas this value is up to 53% for the downdip region. Specifically, the model predicts a LOS displacement of up to ~3 cm for the region downdip of coseismic rupture during the time period before the first SAR image acquisition, which is comparable to the total amount of surface deformation observed in this study starting on

17 November 2017 (Figure S11). Similar to the observations, the model also shows that the surface deformation downdip of the coseismic rupture decays faster than the updip region.

4. Discussion

Our inversions of coseismic displacements due to the 2017 *Mw* 7.3 Sarpol-e Zahab earthquake are generally consistent with earlier studies (e.g., Barnhart et al., 2018; Feng et al., 2018; Liu & Xu, 2019; Nissen et al., 2019; Vajedian et al., 2018), despite the unavoidable epistemic uncertainties related to fault parameterization, inversion regulation, data selection, and so forth (e.g., Wang et al., 2020). Particularly, all the models show that the 2017 Sarpol-e Zahab rupture was along a nearly north-south trending low-angle thrust fault, although the surface expressions of fault and fold in this area trend in a more northwesterly direction. All these slip models also show that the major moment release during the 2017 Sarpol-e Zahab earthquake was concentrated in a depth range between 10 and 20 km, which is well beneath the sediment-basement boundary at 6–10 km in this region. In addition, all these slip models are characterized by nearly equal amounts of thrust and dextral slip, despite the relatively low dip angle (~15–18°). Nonetheless, there are some small-scale differences in the slip distribution among these models. For instance, the models by Barnhart et al. (2018), and Feng et al. (2018) exhibit two distinct slip asperities, while the slip patterns of the models by Vajedian et al. (2018), Nissen et al. (2019), and Liu and Xu (2019) appear simpler. Our model reveals a relatively simple and compact rupture area, while we admit that the detailed slip distribution could depend on the degree of smoothing and regularization in the inversion. The rake of major slip in the model of Barnhart et al. (2018), however, is noticeably smaller than that in all other models. Overall, the 2017 *Mw* 7.3 Sarpol-e Zahab earthquake represents one of the rare cases for which published source models closely agree with each other, likely because of the relatively simple rupture geometry and good coverage of surface deformation measurements.

Historically, there have been no earthquakes of magnitude greater than 7 along the Zagros. Seismic moment release in the past 100 years along the Zagros only accounts for a small fraction of the total strain accumulation determined by geodesy (Masson et al., 2005), leading to the question of how the remaining shortening across the Zagros is accommodated, particularly in the basement. Modeling of coseismic deformation of several moderate-sized earthquakes along the Zagros suggests that most moderate-to-large earthquake ruptures are confined to the middle-to-lower sedimentary cover, while background microseismicity and aftershocks of those events are possibly mostly in the basement (Nissen et al., 2010, 2011, 2014). These observations led to the suggestion that crystalline basement across the Zagros shortens mostly aseismically either through aseismic fault creep accompanied by microseismicity or lower-crustal ductile deformation further to the north (e.g., Nissen et al., 2011). The basement-involved rupture manifested by the 2017 Sarpol-e Zahab earthquake indicates that at least part of the elastic strain accumulation and release along the Zagros resides in the basement, highlighting the potential of seismic hazard from basement faults along the Zagros, particularly when considering that the MFF has a total length of over 1,000 km (Berberian, 1995).

The inversion of coseismic deformation clearly shows that the 2017 Sarpol-e Zahab earthquake did not reach to the surface. Close examination of coseismic interferograms, however, reveals some localized surface deformation in the southwestern corner of the zone of high coseismic surface deformation (near the city of Qasr-e Shirin). The interferograms reveal linear features that are roughly parallel to the surface fold expressions. The largest coseismic offset in LOS direction of the ascending track ASC72 reaches over 6 cm (Figure 11a). Postseismic InSAR time series along profiles normal to these linear features show continued surface creep. During the 1 year after the mainshock, cumulative surface creep (along the LOS direction of the ascending satellite track ASC72) across these secondary faults exceeds 3 cm at some locations. We also note that the most prominent postseismic creep occurs on a segment that did not produce clear coseismic deformation offset (Figure 11b). There are two mechanisms that can produce localized surface deformation during coseismic strains. One is simply due to triggered slip along the secondary faults. Another mechanism involves localized strain due to the reduction of elastic modulus in a fault zone with finite width (e.g., Fialko et al., 2002). Typical widths of the compliant zone inferred from geodesy, seismic guided waves, and tomography range from ~100 m to a few kilometers (Allam et al., 2014; Fialko et al., 2002; Fialko, 2004; Li et al., 1990; Materna & Bürgmann, 2016). The sharp discontinuities in the coseismic deformation field, as well as
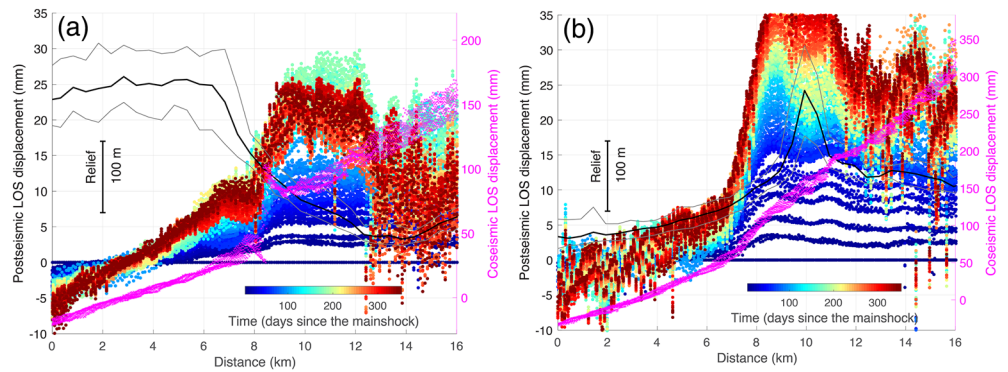
Figure 11. Surface creep across secondary faults southwest of the 2017 Sarpol-e Zahab earthquake along a profile (a) with coseismic offset and (b) without clear coseismic offset (see Location Profiles A and B in Figure 4). Pink dots represent coseismic LOS displacements (for ascending track ASC72) along the profile perpendicular to the surface creep. Colored dots are for the postseismic creep, with the color representing time since the mainshock. Black solid curve represents the surface elevation.

the continued postseismic creep across these features, are diagnostic that the observed strain localization represents triggered slip along secondary faults, rather than the response of a compliant fault zone. The observed postseismic range changes are overall consistent with the coseismic offsets across these features. The lack of a clear signal in the data from the descending tracks across these features, however, makes the interpretation of slip sense not straightforward. Given that the area is in an overall compressional regime, it is possible that the observed range changes distributed over a few kilometers correspond to triggered shallow fault slip on a series of minor reverse faults or flexural slip along bedding planes associated with fold structures. Similar processes have been observed during and after other earthquakes along the Zagros, for example, the 1998 Mw 6.6 Fandoqa (Fielding et al., 2004), the 2005 *Mw* 6.0 Qeshm (Nissen et al., 2007) and the 2013 *Mw* 6.2 Khaki-Shonbe earthquakes (Elliott et al., 2015).

Postseismic deformation following the 2017 Sarpol-e Zahab earthquake has been well documented in several earlier InSAR studies (e.g., Barnhart et al., 2018; Feng et al., 2018; Liu & Xu, 2019; Lv et al. 2020). Yet, as shown in Figure S1, the LOS displacement time series without proper correction for the atmospheric noise can be significantly biased. For this reason, previous studies (e.g., Barnhart et al., 2018; Feng et al., 2018; Liu & Xu, 2019; Lv et al., 2020) using Sentinel-1 data over a similar time period only identified postseismic surface deformation and the corresponding afterslip updip of the coseismic rupture. In this study, we applied the CSS method before the SBAS step to suppress the atmospheric noise that is supposedly random in time. We show that after the CSS, the postseismic LOS displacements from the ascending tracks are clearly characterized by range decrease both updip and downdip of the coseismic rupture, and the LOS displacement time series exhibit temporally coherent decay that is expected from a postseismic relaxation process, even without any temporal smoothing or functional fitting during the SBAS step. Our InSAR time series also suggest that the surface deformation due to afterslip downdip of the coseismic rupture reaches its plateau after ~100 days, while the deformation updip of the coseismic rupture continued to increase until the end of the observation period (Figure 3b). This implies that the downdip afterslip decays faster than the updip region. We find that postseismic deformation 1 year after the 2017 Sarpol-e Zahab earthquake is consistent with an afterslip model with slip concentrated in both updip and downdip fault sections adjoining the coseismic rupture. Little afterslip is resolved in the area of high coseismic slip. The 2017 Sarpol-e Zahab earthquake is therefore a rare case, for which the distribution of afterslip largely follows the predictions from the classical model of a velocity-weakening rupture asperity clearly separated from velocity-strengthening fault sections with distinct geometries. This may be partially attributed to the high-quality InSAR data derived in this study, which significantly improves the model resolution.

Afterslip has been observed following many moderate to large earthquakes in different seismotectonic settings. It represents the response of faults to the stress changes induced by the coseismic rupture (e.g., Bürgmann, 2018). In the framework of rate-and-state friction, earthquakes nucleate in regions of velocity-weakening frictional properties, whereas afterslip occurs on fault sections of velocity

strengthening behavior away from the rupture (Avouac, 2015; Marone, 1998). In this framework, afterslip is expected to mainly occur at the periphery of the coseismic rupture, where the rock friction is velocity strengthening and arrests the seismic rupture. A transition to velocity-strengthening behavior is expected at the downdip portion of seismogenic faults due to increased temperature and pressure (e.g., Marone, 1998). In the upper crust, however, velocity-strengthening fault properties appear limited to specific mineralogies (e.g., clays, serpentinite, and talc), macrostructures and microstructures (e.g., compositional heterogeneity, foliated gouge, and veins), deformation mechanisms (e.g., pressure-solution creep and granular flow), and/or conditions (e.g., near-lithostatic fluid pressure) (e.g., Bürgmann, 2018, and references cited therein). A sharp separation between coseismic slip and afterslip, however, is rarely observed, and afterslip is often inferred to substantially overlap with coseismic ruptures (e.g., Avouac, 2015, and references cited therein). In addition to the limits of resolution of geodetic inversions, another likely explanation involves the role of small-scale spatial (Johnson et al., 2006) or temporal (Hearn et al., 2002) variations in frictional parameters across the fault surface. Numerical simulations have suggested that seismic ruptures could indeed propagate into velocity-strengthening fault areas, when the fault is dynamically weakened by rapid shear heating of pore fluids (Noda & Lapusta, 2013). In such a scenario, one would expect some degree of overlap between afterslip and coseismic rupture.

While afterslip downdip of large earthquake ruptures appears common, what is the cause of velocity-strengthening fault properties updip of the 2017 Sarpol-e Zahab earthquake? Our modeling demonstrates that postseismic deformation in the updip region of the coseismic rupture likely originates from aseismic slip on a subhorizontal plane. Our tests with respect to the fault geometry of the updip afterslip show that the models with relatively deeper transition depths and shallower dips (i.e., >10 km and <10°) fit the data better. In addition, as shown in Figure 5b, the coseismic slip is mostly confined in the depth range between 15 and 20 km; little slip is found at shallower depths above 10 km. The postseismic InSAR LOS displacements derived from the two ascending Sentinel-1 tracks, on the other hand, show that areas of major range decrease closely abut the coseismic slip contours, suggesting a close relationship between coseismic rupture and afterslip. If the afterslip had occurred on a shallower fault plane, the concentration of afterslip would need to be further to the west, leaving a gap between the coseismic rupture and afterslip. Therefore, afterslip updip of the coseismic rupture of the 2017 Sarpol-e Zahab earthquake appears to have occurred on a subhorizontal detachment at a relatively large depth of ~10–14 km, which might correspond to the Hormuz salt layer, a basal evaporite unit deposited in late Proterozoic to early Cambrian through much of the Zagros. Although there is no firm evidence for basal Hormuz salt deposits in the northwestern SFB, mechanical considerations point to an equivalent decoupling horizon in the Lurestan arc either in the sedimentary cover or in the basement that allows for the deformation front to advance southwestward over the Arabian plate via aseismic creep (e.g., McQuarrie, 2004; Motaghi et al., 2017; Teknik & Ghods, 2017; Vergés et al., 2011). Such a mechanically weak layer may act as a barrier to prevent seismic events that nucleated in the sedimentary cover from propagating into the basement, and vice versa (e.g., Nissen et al., 2011). In our modeling, we assume that postseismic deformation following the 2017 Sarpol-e Zahab earthquake is dominantly controlled by afterslip following a rate-strengthening friction; however, ductile shearing of the evaporite layer may have been involved.

Although mechanically afterslip and ductile shearing are different behaviors, it has been shown that crystal-plastic flow within a finite-width shear zone following a power law dependence of strain rate on stress is mathematically equivalent to afterslip following a rate-and-state frictional law (e.g., Barbot et al., 2009; Perfettini & Avouac, 2004). This scenario is consistent with the previous inference that any slip taking place between the metamorphic basement and the overlying sedimentary cover above the Hormuz salt is aseismic (Berberian, 1995). The unique lithological structure of the Zagros could also explain why the afterslip distribution following the 2017 Sarpol-e Zahab earthquake significantly differs from other thrust events of similar magnitudes and tectonic settings; for example, the 1999 Chi-Chi, the 2003 Chengkung, the 2005 Kashmir, and the 2015 Gorkha earthquakes, where afterslip years after the mainshock was all found predominantly downdip of the coseismic rupture (e.g., Hsu et al., 2002, 2009; Wang & Fialko, 2014, 2018; Zhao et al., 2017).

Accompanying the afterslip, the 2017 Sarpol-e Zahab earthquake also produced a large number of aftershocks during the InSAR observation period. Despite the relatively poor automated locations of earthquakes in the Zagros, the earthquake catalog used in this study (from the Iranian Seismic Center) shows that most of

the aftershocks in the first year after the 2017 Sarpol-e Zahab mainshock surround the area of high coseismic slip (Figures 5b and 7). This is somewhat expected, because of the stress increase at the periphery of the coseismic rupture (Figures 7c and 7d). The mechanisms of aftershocks, particularly their relationship with postseismic deformation processes, however, remains unclear. One popular model suggests that aftershocks result from the direct effect of coseismic stress change on a population of nucleating faults with a rate-weakening rheology (Dieterich, 1994). In this model, aftershocks and afterslip are not expected to follow the same temporal evolution, as they represent different physical responses to the coseismic stress change. On the other hand, it has been suggested that aftershocks represent velocity-weakening asperities embedded in a dominantly velocity-strengthening fault and are directly triggered by afterslip; thus, they share similar spatial and temporal evolution patterns (Perfettini et al., 2018; Perfettini & Avouac, 2004). In this study, we show that the aftershocks and surface displacements both updip and downdip of the coseismic rupture follow similar temporal patterns, suggesting that afterslip may indeed have played a direct role in driving the occurrence of aftershocks.

In this study, we estimate the frictional properties of the velocity-strengthening fault sections that experience afterslip in the rate-and-state framework using the surface deformation data. As shown in Equation 2, under the rate-strengthening simplification, the slip rate at the onset of afterslip depends on initial slip rate V_0, the value of a in the rate-and-state friction law, the effective normal stress σ, and the coseismic stress change $\Delta\tau$. There are different explanations about the physical meaning of V_0. Some authors suggest that V_0 should be thought of as a rock property that controls the timescale of afterslip, so it has nothing to do with the actual preearthquake fault slip history (e.g., Barbot et al., 2009). In contrast, others suggest that V_0 should be the preearthquake slip rate (e.g., Johnson et al., 2006; Perfettini & Avouac, 2007). Since Equation 2 is a general expression of fault slip rate based on the rate-and-state frictional law, which relates the coefficient of friction to the sliding velocity of the slider in a spring-slider system, the "initial" velocity on the right-hand side of the equation should be the fault slip rate right before the coseismic shear stress change is applied, that is, the preearthquake slip rate. However, due to the earthquake nucleation, dynamic stress perturbation and weakening, and external loading from viscoelastic relaxation shortly after the earthquake, the slip rate right before the occurrence of afterslip shown in Equation 2 could exceed the interseismic loading rate V_{pl} over a long period (Perfettini & Avouac, 2007). Therefore, instead of assuming V_0 to be the same as the interseismic loading rate V_{pl} (e.g., Johnson et al., 2006), we leave it as a free parameter.

The results show a strong trade-off between V_0 and $a\sigma$. For a wide range of tested values that yield relatively good fitting to the observations, the distribution of V_0 seems to be linearly correlated with $a\sigma$. This is somewhat expected, as $\sinh x \sim x$ for small value of x. Despite the strong trade-off between V_0 and $a\sigma$, all the models yielding acceptable data fitting prefer a relatively high value of V_0 (on the order of m/year). Specifically, the model that yields the best fitting LOS displacement time series for the ascending track ASC72 has $V_0 = 1.42$ m/year for the updip section of the fault. This is substantially higher than the overall convergence rate of ~4 mm/year across the Zagros (Hessami et al., 2006; Vernant et al., 2004), which is further partitioned between multiple faults and folds in the mountain range. To test if such a large value of is required by the data, we run another test by setting $V_0 = 5$ mm/year, a velocity comparable to the interseismic loading rate across the faults in the SFB. We find that the model with such a small value of initial velocity V_0 would significantly underpredict the surface deformation updip of the coseismic rupture, regardless of other parameters.

High values of V_0 have also been documented in the modeling of the postseismic GPS data following the 1992 Landers earthquake (Perfettini & Avouac, 2007), in which the preferred initial velocity is as large as 100 mm/year. What causes such large preearthquake slip rates before the Landers and the 2017 Sarpol-e Zahab earthquakes remains unclear. In addition to the possibilities (e.g., earthquake nucleation, dynamic stress perturbation, and loading from underneath viscoelastic relaxation shortly after the earthquake) discussed in Perfettini and Avouac (2007), foreshock excitation might be another effective way to enhance the fault slip rate leading to the mainshock. For the 2017 Sarpol-e Zahab earthquake, a series of $M4$–5 earthquakes had occurred within a few hours before the Mw 7.3 mainshock, with the closest one being only ~43 min before mainshock (Nissen et al., 2019). It is possible that the stress change from these aftershocks enhanced the creep rate on the fault portions with velocity-strengthening friction, leading to a higher value V_0 of compared to the long-term interseismic creep rate.

In the above postseismic deformation models, we have assumed that the postseismic deformation 1 year after the 2017 Sarpol-e Zahab earthquake is purely due to afterslip. This is in contrast to Lv et al. (2020), who suggest that the postseismic surface deformation from 6 months to 2.5 years after the 2017 Sarpol-e Zahab earthquake contained significant contributions from viscoelastic relaxation of the lower crust and upper mantle. Using a rheological structure similar to Lv et al. (2020), which consists of a Maxwell fluid with an effective viscosity of 1×10^{19} Pa s in the lower crust between 25 and 45 km underlain by a Maxwell-fluid upper mantle with an effective viscosity of 3×10^{19} Pa s, we show that LOS displacements during the InSAR observation period in this study (i.e., 0–1 year after the mainshock) for all four satellite tracks are less than 1 cm, and the spatial pattern of LOS deformation is in significant contrast to the observations (Figure S12). The surface deformation resulting from the viscoelastic relaxation during the time period considered as viscoelastic relaxation in Lv et al. (2020), that is, 6 months to 2.5 years after the mainshock, is even smaller. Our modeling shows that with a lower crustal viscosity of 1×10^{20} Pa s, a more typical value for the lower crust in relatively young deformation zones (e.g., Bürgmann & Dresen, 2008; Thatcher & Pollitz, 2008; Wright et al., 2013), the surface LOS displacements predicted by the viscoelastic relaxation models are less than 5 mm for all four satellite tracks (Figure S13). This is consistent with Barnhart et al. (2018), who also found that the viscoelastic relaxation due to the 2017 Sarpol-e Zahab earthquake during the InSAR observation period was negligible. Furthermore, we have shown that the observed surface deformation can be well explained by afterslip models based on both kinematic afterslip inversion and numerical simulation of stress-driven afterslip without invoking viscoelastic relaxation.

5. Conclusions

With more than 600 fatalities in Iran and Iraq, the 2017 *Mw* 7.3 Sarpol-e Zahab earthquake was the largest instrumentally recorded seismic event along the Zagros mountain range. Similar to most previous large earthquakes along the Zagros, the 2017 Sarpol-e Zahab earthquake did not break to the surface, making the interpretation of its seismogenic structure elusive. In this study, we use Sentinel-1 InSAR to study the coseismic and postseismic deformation due to this event. Thanks to the arid environment and sparse vegetation in the epicentral area, both the coseismic and postseismic deformation of the 2017 Sarpol-e Zahab earthquake are well imaged by Sentinel-1 InSAR observations from four different look directions, which allowed us to tightly constrain the fault geometry and slip distribution of the 2017 Sarpol-e Zahab earthquake. We find that even though most surface expressions (i.e., faults and folds) in this area trend in a northwest-southeast direction, the 2017 Sarpol-e Zahab event ruptured a nearly north-south trending plane (strike = 356°) that gently dips to the east (dip angle = 17°). The coseismic rupture is characterized by nearly equal amounts of thrust and dextral motion distributed on an ~40-km-long and 15-km-wide fault plane, with most of the seismic moment release concentrated in a depth range between 15 and 21 km, which is beneath the boundary between the Phanerozoic sedimentary cover and underlying Proterozoic basement. The 2017 Sarpol-e Zahab earthquake therefore highlights the importance of basement faults in accommodating crustal shortening across the Zagros.

Data from all four Sentinel-1 tracks also reveal robust postseismic deformation during the ~12 months after the mainshock. We have shown that with appropriate corrections for atmospheric noise, the Sentinel-1 InSAR data clearly reveal postseismic deformation both to the west and east of the coseismic rupture, whereas previous studies with similar data only identified the western zone. Kinematic inversions show that the observed postseismic InSAR LOS displacements are well explained by oblique (thrust + dextral) afterslip both updip and downdip of the coseismic slip area. The dip angle of the shallow afterslip fault plane is found to be significantly smaller than that of the coseismic rupture, corresponding to a shallowly dipping detachment located near the base of the sediments. The postseismic deformation data are consistent with stress-driven afterslip models, assuming that the afterslip evolution is governed by rate-and-state friction. Assuming a rate-strengthening friction, the preferred value of $a\sigma$ for the updip afterslip zone is ~30–40 times higher than that of the downdip afterslip zone. The contrast in the frictional properties updip and downdip of the coseismic rupture is likely attributed to the difference in fault zone materials and physical conditions at different depths along the Zagros. In particular, the updip afterslip occurs along a subhorizontal plane at a depth of >10 km, which could be related to the Cambrian Hormoz evaporite deposit layer that behaves as a mechanically weak layer to decouple the deformation of underlying crystalline basement from above. In

contrast, afterslip downdip of the coseismic rupture may be mostly controlled by the increased temperature and pressure, which favor stable sliding, as has been found in other continental earthquakes of similar tectonic settings.

Data Availability Statement

Postseismic InSAR time series derived from this study are archived at Zenodo (https://zenodo.org/record/4025068#.X1vxH5NKgyq) The Common-Scene-Stacking code (Matlab Code for Atmospheric Noise Depression: MCANDIS) used to mitigate the InSAR atmospheric noise can be downloaded from Zenodo (https://zenodo.org/record/4025100#.X1vGMC2z1yo). Aftershock catalog used in this study is from Iranian Seismic Center (ISC) (http://irsc.ut.ac.ir).

References

Allam, A. A., Ben-Zion, Y., Kurzon, I., & Vernon, F. (2014). Seismic velocity structure in the Hot Springs and trifurcation areas of the San Jacinto fault zone, California, from double-difference tomography. *Geophysical Journal International*, *198*(2), 978–999. https://doi.org/10.1093/gji/ggu176

Avouac, J.-P. (2015). From geodetic imaging of seismic and aseismic fault slip to dynamic modeling of the seismic cycle. *Annual Review of Earth and Planetary Sciences*, *43*(1), 1–39. https://doi.org/10.1146/annurev-earth-060614-105302

Barbot, S., Fialko, Y., & Bock, Y. (2009). Postseismic deformation due to the M_w 6.0 2004 Parkfield earthquake: Stress-driven creep on a fault with spatially variable rate-and-state friction parameters. *Journal of Geophysical Research*, *114*, B07405. https://doi.org/10.1029/2008JB005748

Barbot, S., Moore, J. D. P., & Lambert, V. (2017). Displacement and stress associated with distributed anelastic deformation in a half-space. *Bulletin of the Seismological Society of America*, *107*(2), 821–855. https://doi.org/10.1785/0120160237

Barnhart, W. D., Brengman, C. M. J., Li, S., & Peterson, K. E. (2018). Ramp-flat basement structures of the Zagros Mountains inferred from co-seismic slip and afterslip of the 2017 M_w7.3 Darbandikhan, Iran/Iraq earthquake. *Earth and Planetary Science Letters*, *496*, 96–107. https://doi.org/10.1016/j.epsl.2018.05.036

Berardino, P., & Fornaro, G. (2002). A new algorithm for surface deformation monitoring based on small baseline differential SAR interferograms. *IEEE Transactions on Geoscience and Remote Sensing*, *40*(11), 2375–2383. https://doi.org/10.1109/TGRS.2002.803792

Berberian, M. (1995). Master "blind" thrust faults hidden under the Zagros folds: Active basement tectonics and surface morphotectonics. *Tectonophysics*, *241*(3–4), 193–224. https://doi.org/10.1016/0040-1951(94)00185-C

Bürgmann, R. (2018). The geophysics, geology and mechanics of slow fault slip. *Earth and Planetary Science Letters*, *495*, 112–134. https://doi.org/10.1016/j.epsl.2018.04.062

Bürgmann, R., & Dresen, G. (2008). Rheology of the lower crust and upper mantle: Evidence from rock mechanics, geodesy, and field observations. *Annual Review of Earth and Planetary Sciences*, *36*(1), 531–567. https://doi.org/10.1146/annurev.earth.36.031207.124326

Bürgmann, R., Ergintav, S., Segall, P., Hearn, E. H., McClusky, S., Reilinger, R., et al. (2002). Time-dependent distributed afterslip on and deep below the Izmit earthquake rupture. *Bulletin of the Seismological Society of America*, *92*(1), 126–137. https://doi.org/10.1785/0120000833

Chen, C. W., & Zebker, H. A. (2001). Two-dimensional phase unwrapping with use of statistical models for cost functions in nonlinear optimization. *Journal of the Optical Society of America A*, *18*, 338–351.

Chen, K., Xu, W., Mai, P. M., Gao, H., Zhang, L., & Ding, X. (2018). The 2017 Mw 7.3 Sarpol Zahāb Earthquake, Iran: A compact blind shallow-dipping thrust event in the mountain front fault basement. *Tectonophysics*, *747*, 108–114. https://doi.org/10.1016/j.tecto.2018.09.015

Dieterich, J. (1994). A constitutive law for rate of earthquake production and its application to earthquake clustering. *Journal of Geophysical Research: Solid Earth*, *99*(B2), 2601–2618. https://doi.org/10.1029/93JB02581

Elliott, J. R., Bergman, E. A., Copley, A. C., Ghods, A. R., Nissen, E., Oveisi, B., et al. (2015). The 2013 *Mw* 6.2 Khaki-Shonbe (Iran) earthquake: Insights into seismic and aseismic shortening of the Zagros sedimentary cover. *Earth and Space Science*, *2*, 435–471. https://doi.org/10.1002/2015EA000098

Emami, H., Vergés, J., Nalpas, T., Gillespie, P., Sharp, I., Karpuz, R., et al. (2010). Structure of the mountain front flexure along the Anaran anticline in the Pusht-e Kuh Arc (NW Zagros, Iran): Insights from sand box models. *Geological Society, London, Special Publications*, *330*(1), 155–178. https://doi.org/10.1144/SP330.9

Feng, W., Samsonov, S., Almeida, R., Yassaghi, A., & Zheng, W. (2018). Geodetic constraints of the 2017 *Mw*7.3 Sarpol Zahab, Iran earthquake, and its implications on the structure and mechanics of the Northwest Zagros thrust-fold belt. *Geophysical Research Letters*, *45*, 6853–6861. https://doi.org/10.1029/2018GL078577

Ferretti, A., Prati, C., & Racca, F. (2000). Nonlinear subsidence rate estimation using permanent scatterers in differential SAR interferometry. *IEEE Transactions on Geoscience and Remote Sensing*, *38*(5), 2202–2212. https://doi.org/10.1109/36.868878

Fialko, Y. (2004). Probing the mechanical properties of seismically active crust with space geodesy: Study of the coseismic deformation due to the 1992 M_w7.3 Landers (southern California) earthquake. *Journal of Geophysical Research*, *109*, B03307. https://doi.org/10.1029/2003JB002756

Fialko, Y., Sandwell, D., Agnew, D., Simons, M., Shearer, P., & Minster, B. (2002). Deformation on nearby faults induced by the 1999 Hector Mine earthquake. *Science*, *297*(5588), 1858–1862. https://doi.org/10.1126/science.1074671

Fielding, E. J., Wright, T. J., Muller, J., Parsons, B. E., & Walker, R. (2004). Aseismic deformation of a fold-and-thrust belt imaged by synthetic aperture radar interferometry near Shahdad, southeast Iran. *Geology*, *32*(7), 577. https://doi.org/10.1130/G20452.1

Gombert, B., Duputel, Z., Shabani, E., Rivera, L., Jolivet, R., & Hollingsworth, J. (2019). Impulsive Source of the 2017 MW=7.3 Ezgeleh, Iran, Earthquake. *Geophysical Research Letters*, *46*, 5207–5216. https://doi.org/10.1029/2018GL081794

Hearn, E. H., Bürgmann, R., & Reilinger, R. E. (2002). Dynamics of İzmit earthquake postseismic deformation and loading of the Düzce earthquake hypocenter. *Bulletin of the Seismological Society of America*, *92*(1), 172–193. https://doi.org/10.1785/0120000832

Hessami, K., Koyi, H. A., Talbot, C. J., Tabasi, H., & Shabanian, E. (2001). Progressive unconformities within an evolving foreland fold-thrust belt, Zagros Mountains. *Journal of the Geological Society*, *158*(6), 969–981. https://doi.org/10.1144/0016-764901-007

Hessami, K., Nilforoushan, F., & Talbot, C. J. (2006). Active deformation within the Zagros Mountains deduced from GPS measurements. *Journal of the Geological Society*, *163*(1), 143–148. https://doi.org/10.1144/0016-764905-031

Hollingsworth, J., Jackson, J., Walker, R., & Nazari, H. (2008). Extrusion tectonics and subduction in the eastern South Caspian region since 10 Ma. *Geology*, *36*(10), 763–764. https://doi.org/10.1130/G25008A.1

Hooper, A., Bechor, N., & Zebker, H. (2007). Persistent scatterer interferometric synthetic aperture radar for crustal deformation analysis, with application to Volcán Alcedo, Galápagos. *Journal of Geophysical Research*, *112*, B07407. https://doi.org/10.1029/2006JB004763

Hsu, Y.-J., Bechor, N., Segall, P., Yu, S.-B., Kuo, L.-C., & Ma, K.-F. (2002). Temporal and spatial variations of post-seismic deformation following the 1999 Chi-Chi, Taiwan earthquake. *Geophysical Research Letters*, *29*(16), 1754. https://doi.org/10.1029/2002GL014967

Hsu, Y.-J., Simons, M., Avouac, J.-P., Galetzka, J., Sieh, K., Chlieh, M., et al. (2006). Frictional afterslip following the 2005 Nias-Simeulue earthquake, Sumatra. *Science*, *312*(5782), 1921–1926. https://doi.org/10.1126/science.1126960

Hsu, Y.-J., Yu, S. B., & Chen, H.-Y. (2009). Coseismic and postseismic deformation associated with the 2003 Chengkung, Taiwan, earthquake. *Geophysical Journal International*, *176*(2), 420–430. https://doi.org/10.1111/j.1365-246X.2008.04009.x

Jahani, S., Callot, J.-P., de Lamotte, D. F., Letouzey, J., & Leturmy, P. (2007). The salt diapirs of the eastern Fars Province (Zagros, Iran): A brief outline of their past and present. In *Thrust belts and foreland basins* (pp. 289–308). Berlin, Heidelberg: Springer. https://doi.org/10.1007/978-3-540-69426-7_15

Johnson, K. M., Bürgmann, R., & Larson, K. (2006). Frictional properties on the San Andreas Fault near Parkfield, California, inferred from models of afterslip following the 2004 earthquake. *Bulletin of the Seismological Society of America*, *96*(4B), S321–S338. https://doi.org/10.1785/0120050808

Jónsson, S., Zebker, H., Segall, P., & Amelung, F. (2002). Fault slip distribution of the 1999 *Mw* 7.1 Hector Mine, California, earthquake, estimated from satellite radar and GPS measurements. *Bulletin of the Seismological Society of America*, *92*(4), 1377–1389. https://doi.org/10.1785/0120000922

Karasözen, E., Nissen, E., Bergman, E., & Ghods, A. (2019). Seismotectonics of the Zagros (Iran) from orogen-wide, calibrated earthquake relocations. *Journal of Geophysical Research: Solid Earth*, *124*, 9109–9129. https://doi.org/10.1029/2019JB017336

Lange, D., Bedford, J. R., Moreno, M., Tilmann, F., Baez, J. C., Bevis, M., & Krüger, F. (2014). Comparison of postseismic afterslip models with aftershock seismicity for three subduction-zone earthquakes: Nias 2005, Maule 2010 and Tohoku 2011. *Geophysical Journal International*, *199*(2), 784–799. https://doi.org/10.1093/gji/ggu292

Li, Y. G., Leary, P., Aki, K., & Malin, P. (1990). Seismic trapped modes in the Oroville and San Andreas Fault zones. *Science*, *249*(4970), 763–766. https://doi.org/10.1126/science.249.4970.763

Liu, X., & Xu, W. (2019). Logarithmic model joint inversion method for coseismic and postseismic slip: Application to the 2017 *Mw* 7.3 Sarpol Zahāb earthquake, Iran. *Journal of Geophysical Research: Solid Earth*, *124*, 12,034–12,052. https://doi.org/10.1029/2019JB017953

Lv, X., Amelung, F., Shao, Y., Ye, S., Liu, M., & Xie, C. (2020). Rheology of the Zagros Lithosphere from post-seismic deformation of the 2017 Mw7.3 Kermanshah, Iraq, Earthquake. *Remote Sensing*, *12*(12). https://doi.org/10.3390/rs12122032

Marone, C. (1998). The effect of loading rate on static friction and the rate of fault healing during the earthquake cycle. *Nature*, *391*(6662), 69–72. https://doi.org/10.1038/34157

Masson, F., Chéry, J., Hatzfeld, D., Martinod, J., Vernant, P., Tavakoli, F., & Ashtiani, M. G. (2005). Seismic versus aseismic deformation in Iran inferred from earthquakes and geodetic data. *Geophysical Journal International*, *160*(1), 217–226. https://doi.org/10.1111/j.1365-246X.2004.02465.x

Materna, K., & Bürgmann, R. (2016). Contrasts in compliant fault zone properties inferred from geodetic measurements in the San Francisco Bay area. *Journal of Geophysical Research: Solid Earth*, *121*, 6916–6931. https://doi.org/10.1002/2016JB013243

McQuarrie, N. (2004). Crustal scale geometry of the Zagros fold-thrust belt, Iran. *Journal of Structural Geology*, *26*(3), 519–535. https://doi.org/10.1016/j.jsg.2003.08.009

McQuarrie, N., Stock, J. M., Verdel, C., & Wernicke, B. P. (2003). Cenozoic evolution of Neotethys and implications for the causes of plate motions. *Geophysical Research Letters*, *30*(20), 2036. https://doi.org/10.1029/2003GL017992

Milliner, C., Bürgmann, R., Inbal, A., Wang, T., & Liang, C. (2020). Resolving the kinematics and moment release of early afterslip within the first hours following the 2016 *Mw* 7.1 Kumamoto earthquake: Implications for the shallow slip deficit and frictional behavior of aseismic creep. *Journal of Geophysical Research: Solid Earth*, *125*, e2019JB018928. https://doi.org/10.1029/2019JB018928

Motaghi, K., Shabanian, E., & Kalvandi, F. (2017). Underplating along the northern portion of the Zagros suture zone, Iran. *Geophysical Journal International*, *210*(1), 375–389. https://doi.org/10.1093/gji/ggx168

Neal, R. M. (2003). Slice sampling. *Annals of Statistics*, *31*(3), 705–767. https://doi.org/10.1214/aos/1056562461

Nissen, E., Ghods, A., Karasözen, E., Elliott, J. R., Barnhart, W. D., Bergman, E. A., et al. (2019). The 12 November 2017 *Mw* 7.3 Ezgeleh-Sarpolzahab (Iran) Earthquake and Active Tectonics of the Lurestan Arc. *Journal of Geophysical Research: Solid Earth*, *124*, 2124–2152. https://doi.org/10.1029/2018JB016221

Nissen, E., Ghorashi, M., Jackson, J., Parsons, B., & Talebian, M. (2007). The 2005 Qeshm Island earthquake (Iran)—A link between buried reverse faulting and surface folding in the Zagros Simply Folded Belt? *Geophysical Journal International*, *171*(1), 326–338. https://doi.org/10.1111/j.1365-246x.2007.03514.x

Nissen, E., Jackson, J., Jahani, S., & Tatar, M. (2014). Zagros "phantom earthquakes" reassessed—The interplay of seismicity and deep salt flow in the Simply Folded Belt? *Journal of Geophysical Research: Solid Earth*, *119*, 3561–3583. https://doi.org/10.1002/2013JB010796

Nissen, E., Tatar, M., Jackson, J. A., & Allen, M. B. (2011). New views on earthquake faulting in the Zagros fold-and-thrust belt of Iran. *Geophysical Journal International*, *186*(3), 928–944. https://doi.org/10.1111/j.1365-246X.2011.5119.x

Nissen, E., Yamini-Fard, F., Tatar, M., Gholamzadeh, A., Bergman, E., Elliott, J. R., et al. (2010). The vertical separation of mainshock rupture and microseismicity at Qeshm island in the Zagros fold-and-thrust belt, Iran. *Earth and Planetary Science Letters*, *296*(3–4), 181–194. https://doi.org/10.1016/j.epsl.2010.04.049

Noda, H., & Lapusta, N. (2013). Stable creeping fault segments can become destructive as a result of dynamic weakening. *Nature*, *493*(7433), 518–521. https://doi.org/10.1038/nature11703

Okada, Y. (1985). Surface deformation due to shear and tensile faults in a half-space. *Bulletin of the Seismological Society of America*, *75*(4), 1135–1154.

Perfettini, H., & Avouac, J. P. (2004). Postseismic relaxation driven by brittle creep: A possible mechanism to reconcile geodetic measurements and the decay rate of aftershocks, application to the Chi-Chi earthquake, Taiwan. *Journal of Geophysical Research*, *109*, B02304. https://doi.org/10.1029/2003JB002488

Perfettini, H., & Avouac, J. P. (2007). Modeling afterslip and aftershocks following the 1992 Landers earthquake. *Journal of Geophysical Research*, *112*, B07409. https://doi.org/10.1029/2006JB004399

Perfettini, H., Avouac, J. P., Tavera, H., Kositsky, A., Nocquet, J. M., Bondoux, F., et al. (2010). Seismic and aseismic slip on the Central Peru megathrust. *Nature*, *465*(7294), 78–81. https://doi.org/10.1038/nature09062

Perfettini, H., Frank, W. B., Marsan, D., & Bouchon, M. (2018). A model of aftershock migration driven by afterslip. *Geophysical Research Letters*, *45*, 2283–2293. https://doi.org/10.1002/2017GL076287

Pirouz, M., Avouac, J.-P., Hassanzadeh, J., Kirschvink, J. L., & Bahroudi, A. (2017). Early Neogene foreland of the Zagros, implications for the initial closure of the Neo-Tethys and kinematics of crustal shortening. *Earth and Planetary Science Letters*, *477*, 168–182. https://doi.org/10.1016/j.epsl.2017.07.046

Ruina, A. (1983). Slip instability and state variable friction laws. *Journal of Geophysical Research*, *88*(B12), 10,359–10,370. https://doi.org/10.1029/JB088iB12p10359

Sandwell, D., Mellors, R., Tong, X., Wei, M., & Wessel, P. (2011). Open radar interferometry software for mapping surface deformation. *Eos, Transactions, American Geophysical Union*, *92*(28), 234. https://doi.org/10.1029/2011EO280002

Schmidt, D. A., & Bürgman, R. (2003). Time-dependent land uplift and subsidence in the Santa Clara valley, California, from a large interferometric synthetic aperture radar data set. *Journal of Geophysical Research*, *108*(B9), 2416. https://doi.org/10.1029/2002JB002267

Sudhaus, H., & Jónsson, S. (2009). Improved source modelling through combined use of InSAR and GPS under consideration of correlated data errors: Application to the June 2000 Kleifarvatn earthquake, Iceland. *Geophysical Journal International*, *176*(2), 389–404. https://doi.org/10.1111/j.1365-246X.2008.03989.x

Teknik, V., & Ghods, A. (2017). Depth of magnetic basement in Iran based on fractal spectral analysis of aeromagnetic data. *Geophysical Journal International*, *209*(3), 1878–1891. https://doi.org/10.1093/gji/ggx132

Thatcher, W., & Pollitz, F. F. (2008). Temporal evolution of continental lithospheric strength in actively deforming regions. *GSA Today*, *18*(4), 4. https://doi.org/10.1130/gsat01804-5a.1

Tymofyeyeva, E., & Fialko, Y. (2015). Mitigation of atmospheric phase delays in InSAR data, with application to the eastern California shear zone. *Journal of Geophysical Research: Solid Earth*, *120*, 5952–5963. https://doi.org/10.1002/2015JB011886

Vajedian, S., Motagh, M., Mousavi, Z., Motaghi, K., Fielding, E., Akbari, B., et al. (2018). Coseismic deformation field of the *Mw* 7.3 12 November 2017 Sarpol-e Zahab (Iran) earthquake: A decoupling horizon in the northern Zagros Mountains inferred from InSAR observations. *Remote Sensing*, *10*(10), 1589. https://doi.org/10.3390/rs10101589

Vergés, J., Saura, E., Casciello, E., Fernàndez, M., Villaseñor, A., Jiménez-munt, I., & García-castellanos, D. (2011). Crustal-scale cross-sections across the NW Zagros belt: Implications for the Arabian margin reconstruction. *Geological Magazine*, *148*(5–6), 739–761. https://doi.org/10.1017/S0016756811000331

Vernant, P., Nilforoushan, F., Hatzfeld, D., Abbassi, M. R., Vigny, C., Masson, F., et al. (2004). Present-day crustal deformation and plate kinematics in the Middle East constrained by GPS measurements in Iran and northern Oman. *Geophysical Journal International*, *157*(1), 381–398. https://doi.org/10.1111/j.1365-246X.2004.02222.x

Wang, K., Dreger, D. S., Tinti, E., Bürgmann, R., & Taira, T. (2020). Rupture process of the 2019 Ridgecrest, California *Mw* 6.4 foreshock and *Mw* 7.1 earthquake constrained by seismic and geodetic data. *Bulletin of the Seismological Society of America*, *110*(4), 1603–1626. https://doi.org/10.1785/0120200108

Wang, K., & Fialko, Y. (2014). Space geodetic observations and models of postseismic deformation due to the 2005 *M*7.6 Kashmir (Pakistan) earthquake. *Journal of Geophysical Research: Solid Earth*, *119*, 7306–7318. https://doi.org/10.1002/2014JB011122

Wang, K., & Fialko, Y. (2015). Slip model of the 2015 *Mw* 7.8 Gorkha (Nepal) earthquake from inversions of ALOS-2 and GPS data. *Geophysical Research Letters*, *42*, 7452–7458. https://doi.org/10.1002/2015GL065201

Wang, K., & Fialko, Y. (2018). Observations and modeling of coseismic and postseismic deformation due to the 2015 *Mw* 7.8 Gorkha (Nepal) earthquake. *Journal of Geophysical Research: Solid Earth*, *123*, 761–779. https://doi.org/10.1002/2017JB014620

Wang, K., Xu, X., & Fialko, Y. (2017). Improving burst alignment in TOPS interferometry with bivariate enhanced spectral diversity. *IEEE Geoscience and Remote Sensing Letters*, *14*(12), 2423–2427. https://doi.org/10.1109/LGRS.2017.2767575

Wright, T. J., Elliott, J. R., Wang, H., & Ryder, I. (2013). Earthquake cycle deformation and the Moho: Implications for the rheology of continental lithosphere. *Tectonophysics*, *609*, 504–523. https://doi.org/10.1016/j.tecto.2013.07.029

Zhao, B., Bürgmann, R., Wang, D., Tan, K., Du, R., & Zhang, R. (2017). Dominant controls of downdip afterslip and viscous relaxation on the postseismic displacements following the Mw7.9 Gorkha, Nepal, earthquake. *Journal of Geophysical Research: Solid Earth*, *122*, 8376–8401. https://doi.org/10.1002/2017JB014366